Geology, mineralogy, and sulfur isotopic studies of proximal volcanic products at the Tangkuban Parahu Volcano, Indonesia.

Syahreza Saidina Angkasa

Submitted for partial fulfillment of the requirements of doctoral degree

Department of Earth Resource Science
Faculty of International Resource Science

Akita University

May 2019

Supervisor: Prof. Tsukasa Ohba

Abstract

Tangkuban Parahu volcano is one of the most active volcanoes in West Java, Indonesia, although most of the recent eruptions were relatively mild (e.g., 2013 eruption). However, there is still little information from the volcanic products in the proximal area. Here, we provide new documentation from the proximal volcanic succession, including tephra-stratigraphy, componentry analysis, and petrography of volcanic products. Detailed mapping of the proximal area shows that the volcanic products are predominantly composed of an alternation fine-clay and coarse ash, lapilli tuff, and pyroclastic breccia within 10 tephra units. Componentry of ash particles revealed the presence of five components, which associated with hydrothermally altered lithics, oxidized lithics, coherent crystalline lithics, magmatic juvenile and free crystal in entire eruptive products. These indicate that the subvolcanic hydrothermal system has been developed since the Holocene and associated with a continual introduction of magmatic intrusion. Petrographic observation shows the hydrothermal minerals of quartz or silica accompanied by alunite and kaolinite, which represents acidic alteration within the crater-conduit. The presence of the silicified zone indicates that the subvolcanic hydrothermal system plays an essential role as a cap-rock of pressurized gas and steam at depth (200-500 m), whereas magmatic injection caused the vapor plume expansion. Our observation concluded that the proximal volcanic succession captured the evidence of coupled phreatic and phreatomagmatic activities during the latest development of Mt. Tangkuban Parahu.

In order to understand the subvolcanic hydrothermal system condition, we carried out the mineralogy and sulfur isotopic signature of volcanic products from the proximal area of Tangkuban Parahu volcano. X-ray diffraction analysis reveals the majority of the hydrothermal mineral constituent. Silica polymorph (quartz, cristobalite, and tridymite) and alunite are dominant, whereas kaolinite randomly presents in some stratigraphic sections. Jarosite and goethite are abundant in the upper section of composite stratigraphy. The temporal mineralogical changing could reflect the depth of explosion or hydrothermal alteration development below the active craters, where

some jarosite and possibly represent highly oxidized conditions after the emplacement process. From petrographic observation, hydrothermally altered lithics consist of two primary ash particle types; 1) partly altered magmatic glass and 2) selectively to pervasively altered ash fraction. The later ash particles comprise four types hydrothermal mineral assemblages along with two evidence of hydrothermal veinlet feeders. Hydrothermal mineral assemblages are opal, opal + cristobalite + alunite ± kaolinite, quartz + alunite ± kaolinite, and oxidation of alunite + jarosite, whereas the veinlets are silica+alunite-kaolinite-goethite±APS and quartz-pyrite. The accessory minerals (pyrite, chalcopyrite, and enargite) also present in many ash particles. These alteration assemblages are classified as acid-sulfate alteration and argillic alteration, which mostly present at near-surface of geothermal field in calc-alkaline stratovolcanoes. Their presence also possibly rooted in high-temperature magmatic-vapor zone underneath the volcano.

Acknowledgments

The author would like to thank, first of all, to Allah SWT the Most Gracious and Merciful for allowing finishing the doctoral course at Faculty International Resource Science, Akita University. I want to say thanks to my supervisor Prof. Tsukasa Ohba and all professors and staff at Akita University, for their enormous support during the study period.

All petrology and volcanology group members and technical assistant in 2016-2019; for their help and discussion.

Japanese Mobunkagakusho scholarship and New Frontier Leading Program are acknowledged to give full financial support for this project. This project also supported by JSPS Kakenhi; project no. #17K01319 and #15K01245.

Tangkuban Parahu volcano observatory staff (CVGHM) and the Natural Resource Conservation Center (BKSDA, for their assistance in providing logistics and sampling permits during fieldwork.

Faculty members and staff at Universitas Padjadjaran are thanked for providing assistance travel permits of the analyzed samples in this thesis. All Indonesian students and residences in Akita City, for their help and assistance.

Syahrul Syah and Rizky Amanda are thanked for financial and moral supports, which cannot be elaborate only with a single sentence or whole thesis.

Most special appreciation for my best partner, Adiis Retna Utara, who always supports me, especially during the “mental” thesis period. For Omar Salahaddin Angkasa and Syadia Nura Angkasa, happy to see both of you are growing up so well! Now, we are going back home to Indonesia, then three of you can do what you want! I will support everything for three of you in the future!

Lastly, if you (person or/and institution) have not mentioned and feel that you should be acknowledged for this project, then consider yourself acknowledged.

Chapter 1
Introduction

1.1. Project outline

This thesis aims to evaluate the potential role of volcanic products from the phreatic and phreatomagmatic eruptions that commonly contain hydrothermally altered lithics by implementing field and laboratory techniques. The observations are beneficial for providing new volcanological records in volcano-stratigraphy, mineralogy, and sulfur isotope. The data in this thesis was collected from a selected stratovolcano within Sunda volcanic arc, Indonesia, namely Tangkuban Parahu volcano. The volcano has been very active during the last ten years, but there is still little information, explaining the volcanic activity from pre-historic and modern eruptive products. Therefore, the thesis can give a profound contribution to better understand the volcanic unrest in the past, which may deliver the necessary knowledge for future hazard evaluation.

This chapter summarises the motivation, aim, and structure of the project. The general structure of this thesis is based on two central chapters assessing the field and laboratory works. In the second chapter, the field and some of the laboratory works (i.e., tephra stratigraphy, stereoscopic, and petrographic observations) are presented as the general basis of geological understanding, and possible eruption process and history. For the third chapter, it will exclusively deliberate the mineralogy, textural variation, and sulfur isotopic signatures from hydrothermally altered lithics to get a new insight into the condition of the sub-volcanic hydrothermal system throughout the time. Additionally, the geological setting of the Sunda volcanic arc is summarized in this chapter. For more specific geological information of Tangkuban Parahu will be described in the next two chapters, which depends on the context of discussions on each chapter.

1.1.1. Project motivation I – field-based approach

The primary interest of this thesis is to evaluate the mineralogy of volcanic products. However, it is difficult to connect the mineralogy and sulfur isotope results with the available tephra stratigraphy due to insufficient information from the field observation

at the summit crater vicinity. In many previous works, they mostly only introduced brief documentation of stratigraphy (Fig. 1.1) and geological condition at the proximal area (e.g., Stehn, 1929; Silitonga, 1973; Hadisantono et al. 1989; Sutoyo and Hadisantono, 1990). In this context, the presence, significance, and importance of the Tangkuban Parahu proximal volcanic products are still understudied.

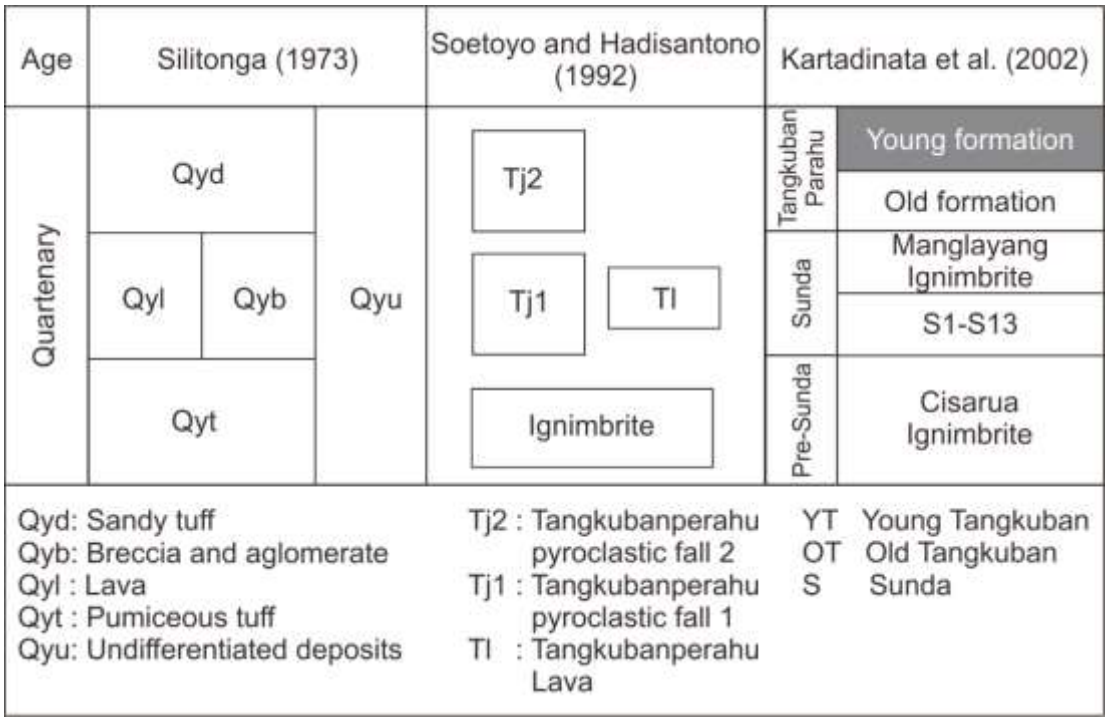

Figure 1.1 Summary of Tangkuban Parahu stratigraphic development from the 1970s to 2002.

A most recent study from Kartadinata et al. (2002) and Kartadinata (2005) (Fig. 1.1 and Fig 1.2) has put an effort to characterize the volcanic products from old (Pliocene-Pleistocene) and young (Holocene) volcanic events. Moreover, Kartadinata et al. (2002) revealed the eruption history for youngest evolution stage of Tangkuban Parahu volcano (Kartadinata et al., 2002; Nasution et al., 2004). The results provided a significant development of Tangkuban Parahu volcano-stratigraphy (Fig 1.1). The volcanic succession comprises two main formations of Old and Young Tangkuban Parahu (OTP and YTP, respectively). OTP Formation (c. 0.1 Ma; Sunardi and Kimura, 1998) was relatively well-studied in Kartadinata et al. (2002) and (2005). Both previous works showed new data of radiocarbon dating, isopach map, and volume estimation from the Old Tangkuban Parahu volcanic products. For YTP Formation, they are mostly provided only brief information on the volcanic products, although the YTP

volcanic products are essential for decoding the recent volcanic activity outputs (e.g., phreatic and phreatomagmatic eruptions). Consequently, fieldwork was conducted to re-observe some outcrops and provide the new stratigraphy from YTP Formation, which mainly situated in the proximal area (see chapter 2).

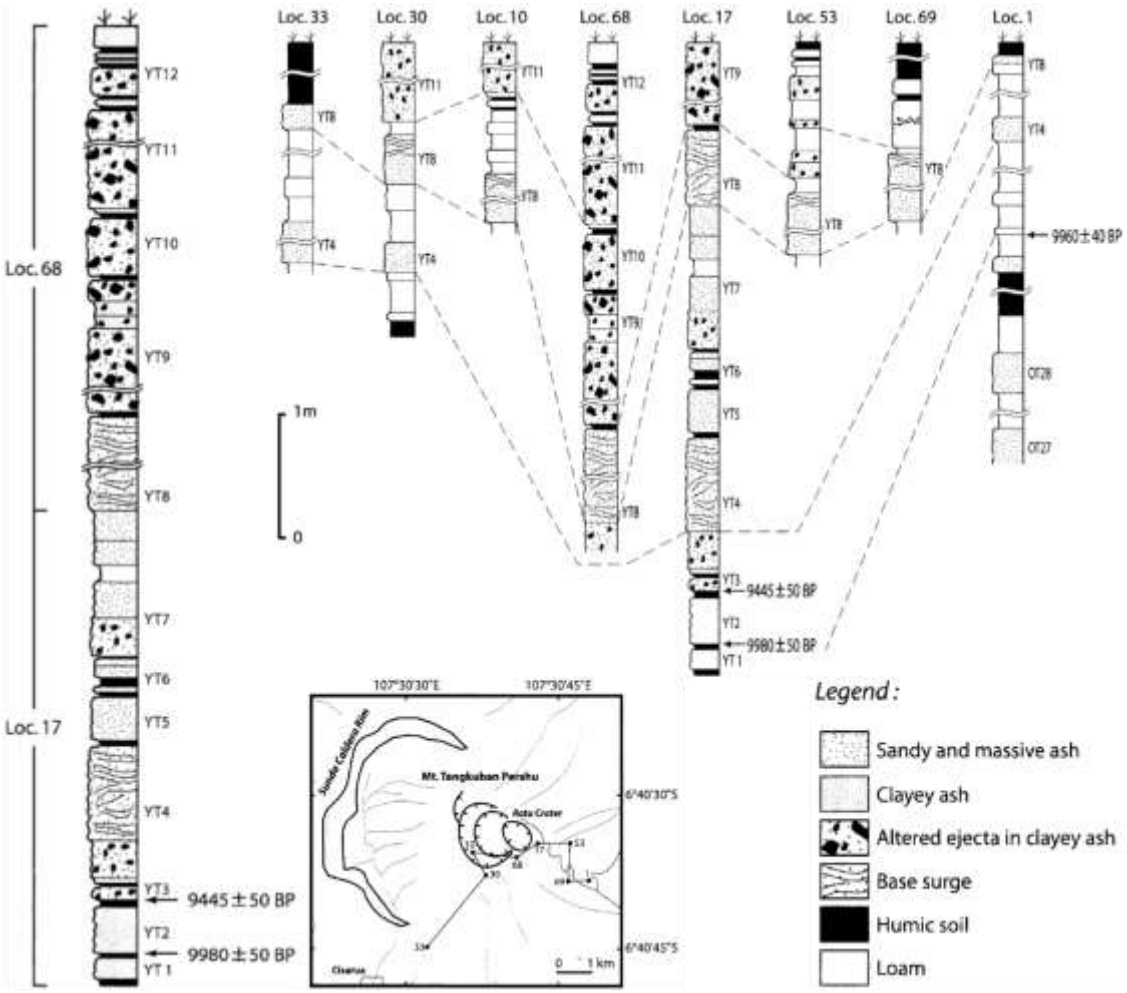

Figure 1.2 The tephra-stratigraphy of Young Tangkuban Parahu formation from the previous research (Kartadinata et al., 2002). The composite tephra succession is ~7 meters in thickness, which mostly comprises the volcanic products from phreatic events younger than 10.000 BP.

1.1.2. Project motivation II – mineralogy and sulfur isotope-based approaches

Mineralogy, textural variation, and sulfur isotopic approaches were motivated by limited documentation of the characteristics of volcanic products from phreatic or hydrothermal and phreatomagmatic or magmatic-hydrothermal eruptions (Brownee and Lawless, 2001). Both eruptions are relatively small and not so attractive to

research. Therefore, it still provides many research questions that can be addressed, specifically in Indonesia. The volcanic products from both eruptions (phreatic and phreatomagmatic) predominantly contain hydrothermally altered lithics (e.g., Nairn et al., 1979), which can be used to estimate the sub-volcanic hydrothermal system below the active craters (Ohba and Kitade et al., 2005). Moreover, mineralogical based observation can give critical information to characterize the sub-volcanic hydrothermal system because the sealing capacity of pressurized fluid below the crater mostly provided by clayey layers or other hydrothermal mineral zonation (e.g., Wright et al., 1985; Pellerin et al., 1996).

In chapter 3, mineralogy and sulfur isotope were carried out from the volcanic products to understand better the condition of Tangkuban Parahu during the pre-historical era (i.e., phreatic and phreatomagmatic events). The focus was chosen to characterize the hydrothermally altered lithics, which is the most abundant component (e.g., volcanic rocks and magmatic juvenile; see chapter 2) in the volcanic products. The hydrothermally altered lithics are still fresh due to less intensity of weathering process and fewer vegetations at the summit of the volcano. In addition, The presence of hydrothermally altered lithics in all volcanic products allowing us to understand the temporal changing of the hydrothermal system within crater-conduit (Ohba and Kitade, 2005; Takahashi et al., 2016) from a material science perspective (Ohba and Nakagawa, 2002; Ohba and Kitade, 2005; Minami et al., 2016).

1.2. Project aims and objectives

The aims and objectives of this project are:

1. To document detail tephra-stratigraphy (e.g., lithological, volcanic facies, internal and external structure).
2. To document mineralogy, textural variation and sulfur isotope from the volcanic products.
3. To better understand the eruption process, mechanism and dynamic from the studied stratigraphy
4. To constraint condition of the subvolcanic hydrothermal system and its role during the eruption process, including zonation and overprinting relationship

Those aims can be achieved by several methods that will describe on methodology section in two central chapters (chapter 2 and 3).

1.3. Geological framework

The following section provides an overview of the geological setting from the studied area. This section intention is to give a brief introduction about the regional context since the Tangkuban Parahu volcano is a part of the volcanic chain within the larger Sunda volcanic arc.

1.3.1. Sunda volcanic arc

Sunda volcanic arc is located along the convergent margin of Indo-Australian and Eurasian plates with 6-7 cm/yr (centimeter/year) of movement speed (Fig. 1.3A). The Indo-Australian plate has been continuously subducted to the Eurasian plate since ca. 45 Ma (Tregoning et al., 1994; Hall, 2002) at South-East Asia region. Subducted slab beneath Sumatra is oblique, while the slab beneath the Java Island is steepened (ca. 60º) to the northward dipping trend (Fig 1.3B) with Benioff zones at a depth of ca. 100 km (Whitford, 1979; Curray 1989).

The active volcanic system distributed throughout Western Indonesia (Sumatra and Java) and the Andaman Islands (Hall and Smyth, 2008) contributes a ~80% of total active volcanoes within the Indonesia archipelago (Fig. 1.2A). Petrology of volcanic rocks (i.e., lava) was extensively studied starting from the late 1970s from Pleistocene to recent volcanism (e.g., Whitford, 1975; Nicholls et al., 1980; Wheller et al., 1987; Edwards et al., 1990; Gasparon et al., 1994; Gertisser and Keller, 2003; Handley et al., 2006) with most comprehensive range of geochemical affinity from any other volcanic arcs or orogenic settings (Wheller et al., 1987). The extrusive rocks are range from tholeiitic to high-alkaline leucitic, although most of the volcanic rocks are predominantly fall into calc-alkaline basaltic-andesite and andesite (Nicholls and Whitford 1976; Handley, 2006).

1.3.2. Volcanoes in West Java

Many of active and extinct volcanoes in West Java province are still poorly studied, as a result in this section will only provide information from relatively well-characterized volcanoes. West Java Province hosts nine active volcanoes, which has been continuously erupting in the last 10.000 years. The volcanoes divided into two division of volcanic chains (front and rear arc; e.g., Sendjadja et al., 2009).

Front arc volcanoes include Cikuray, Papandayan, Galunggung, Guntur, Patuha and Papadayan, whereas the rear arc (behind the front) volcanoes consist of Ciremai, Tampomas, and Tangkuban Parahu (Fig 1.3C). Two distinct of front arc volcanoes were provided by Dempsey, 2013 from elemental ratios against SiO_2 content of lava and some pyroclastic rocks. Galungung, Cikuray and Guntur tholeiitic generally contain rocks with lower SiO_2 display minor enrichment of K_2O, Rb, Th, and Rb/Sr. In contrast, Papandayan, Patahu and Guntur calc-alkaline contain very few volcanic rocks with < 55 wt% SiO_2 and more enriched in K_2O, Rb, Th, and Rb/Sr. Both classifications were postulated to be contaminated by upper-crust material (i.e., Sundaland Siliciclastics and overlying basement) (Gertiser and Keller, 2003; Handley, 2006; Sendjadja et al., 2009; Handley et al., 2011; Dempsey, 2013), although this is still poorly understood.

Gede volcano was excluded from those classifications, although it is also classified as a front-arc volcano in many local articles (see CVGHM, 2016). The volcano is relatively dormant in modern times but had violent eruptions in the pre-historical era. Recent general petrological documentation from Belousov et al. (2015) shows the majority of volcanic rocks fall into andesite and basaltic-andesite classification, with a variation of high-alumina basalts that represent typical volcanic rock at the subduction zone (Winter, 2001). Moreover, the dacitic composition also occurs from the 1200 years BP pyroclastic density current (Beulosov et al., 2015).

The rear arc margin, specifically for Tangkuban Parahu volcano, the volcanic rocks (i.e., lava; pyroclastic rock) are divided into two types of volcanic products; 1) volcanic rocks related with Sunda volcano, so-called the Sunda volcanic, and 2) volcanic rocks related with the Tangkuban Parahu volcano. Lavas are basalt to dacite (SiO_2 contents,

51-63 wt%) in composition (Sunardi and Kimura, 1998), which also falls into tholeiitic and calc-alkaline suites and covers the medium-K to high-K suites (Sunardi and Kimura 1998). Calc-alkaline volcanic rocks are mostly consistent with R-type (reverse-zoning), whereas the tholeiite suite lava corresponds well with the N-type (normal zoning) from Sakuyama (1979 and 1981) classification.

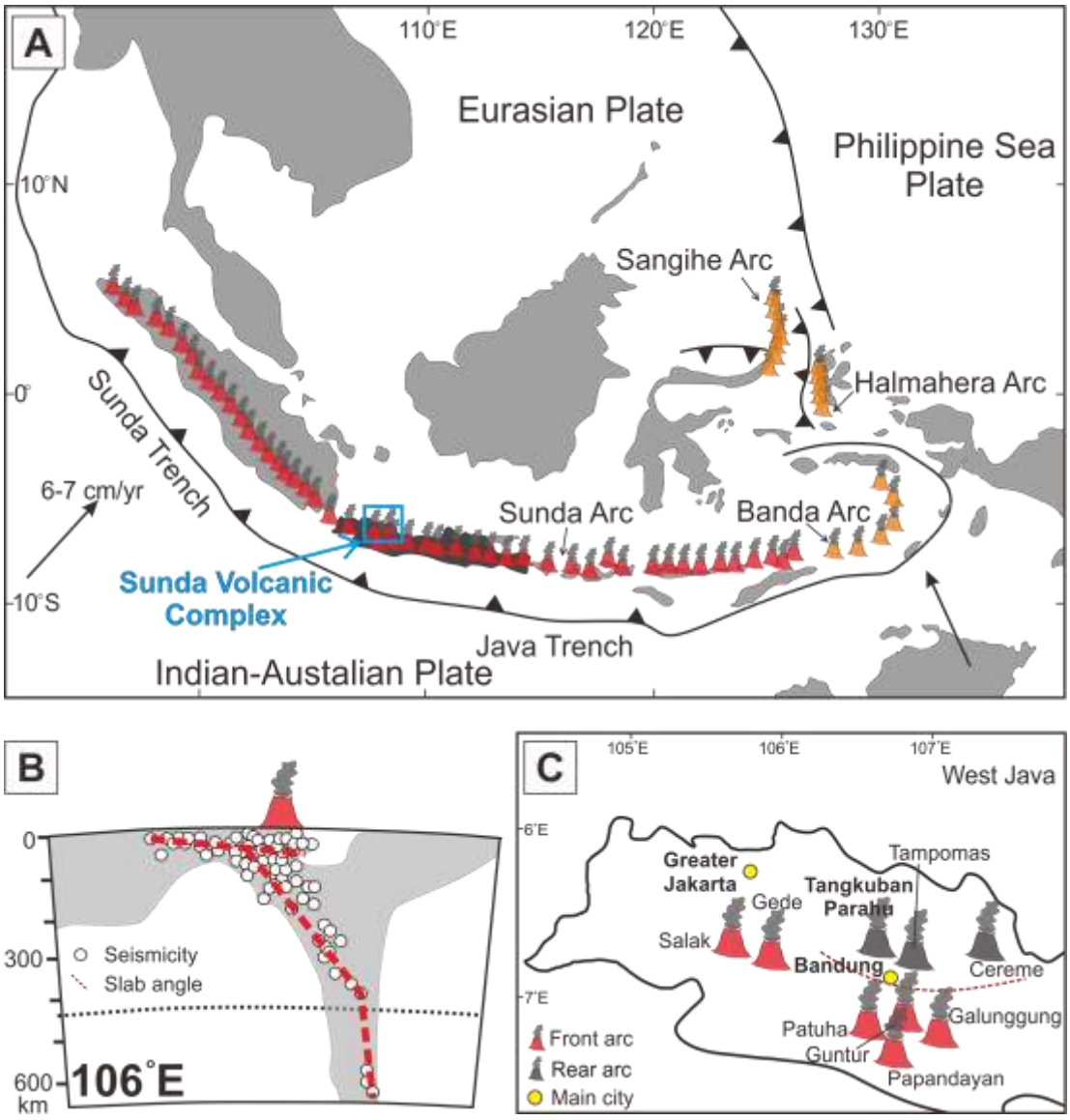

Figure 1.3 Map showing the tectonic of Indonesia archipelago as a result of Indo-Australian subduction to the Eurasian plate. A) The ring of fire (volcanoes) is widespread from the west (Sumatra) to East (Timor and Sulawesi). The blue square is showing the location of the Tangkuban Parahu volcano part of the Sunda Volcanic Complex (SVC). B) Subduction slab profiles underneath the West Java Province from Widiyantoro et al. (2011) and modified after Dempsey (2013). C) Detail location of volcanoes at West Java consisting of front arc volcano (e.g., Guntur, Galunggung) as well as the rear margin of a volcanic chain (e.g., Tangkuban Parahu).

1.4. Outline of the thesis

The thesis includes detailed field observation and laboratory works (componentry, mineralogy, petrography, and sulfur isotope) of the proximal volcanic succession at the Tangkuban Parahu Volcano. The outline of this thesis;

Chapter 1: Introduction, including project outline and motivation, geological setting of Sunda volcanic arc together with the general information of volcanoes in West Java province, and thesis outline.

Chapter 2: It consists of a general geological understanding of Tangkuban Parahu volcano. This chapter provides the proximal tephra stratigraphy, componentry analysis, and petrography of proximal volcanic products.

Chapter 3: Mineralogy and sulfur isotope studies of Tangkuban Parahu volcanic products. This chapter exclusively deliberates mineralogical variations from the hydrothermally altered lithics, including the sulfur isotopic values from sulfate and sulfide minerals.

Appendices: The appendices include the stratigraphic comparison with the previous study and mineral chemistry of selected minerals in volcanic products.

Chapter 2.
Tephra-stratigraphy and ash componentry studies of volcanic products at proximal at Tangkuban Parahu volcano, Indonesia: an insight to Holocene volcanic activity.

2.1. Introduction

The phreatic or hydrothermal eruption is a typical volcanic event associated with the rapid release of a confined pocket of pressurized flashing water and steam below the crater in many stratovolcanoes worldwide (e.g., Wohletz and Heiken, 1992; Brownee and Lawless, 2001). In some cases, phreatic eruption is related to the heated hydrous-rich zone (e.g., aquifer, subvolcanic hydrothermal system) by a magmatic intrusion, which leads to vapor expansion, and the boiling of pore fluid and hydrous minerals (Brownee and Lawless, 2001; Jamveit et al., 2004; Lowernstern et al., 2018). The significance of phreatic eruption is that the explosion occurs unexpectedly, thus may cause a lethal proximal hazard due to the absence of precursory signals from geophysical and geochemical monitoring (Barberi, 1992; Marini, 1996). The most recent dramatic example is the 2014 eruption of Mt. Ontake, Japan, with a total of 63 people dead or missing (Sanno et al., 2015; Oikawa et al., 2016).

Phreatic deposits are mostly identified from field observation, presented as white and yellow color tephra succession with a range of grain size from ash to block fragment (Maeno et al., 2016; Oikawa et al., 2018). There are also an increasing number of studies using componentry analysis of volcanic products to classify phreatic explosion from phreatomagmatic eruption (e.g., Suzuki et al., 2013; Pardo et al., 2013; Alvarado et al., 2016). Additionally, phreatic and phreatomagmatic eruptive products contain hydrothermally altered lithic fragments, which have particular importance as they provide direct evidence for the subvolcanic hydrothermal conditions within the crater-conduit (e.g., Ohba and Kitade, 2005; Ohba et al., 2007). Consequently, careful observation of ash particles may give a valuable constraint on the process and an important role of the subvolcanic hydrothermal system leading to a volcanic eruption (Ohba and Kitade., 2005; Ohba et al., 2007; Minami et al., 2016). More detailed

observation on hydrothermally altered lithic fragments will be provided in the next chapter 3.

At Tangkuban Parahu volcano, an exotic surface manifestation within the active craters has become an attraction for many locals and international tourists to visit and stay in the vicinity of the volcano. Therefore, even a small-scale eruption can cause inevitable casualties for society and infrastructures. Nineteen explosions were reported from 1829 to 2004, and the last eruption occurred in 2013 (CVGM report, 2016). However, it was not clear whether those volcanic activities were purely phreatic or phreatomagmatic. Moreover, it is challenging to recognize the historical and pre-historical tephra succession due to scarce documentation of the volcanic products (e.g., Silitonga, 1973; Kusumadinata, 1979; Koesoemadinata 1992; Soetoyo and Hadisantono, 1992; Sunardi and Kimura, 1998; Kartadinata et al., 2002). Therefore, this study aims to document the detailed tephra stratigraphy and composition of the volcanic products at Mt. Tangkuban Parahu, Indonesia.

The main focus was on the tephra succession at the proximal area, which captured the eruption history and mechanism in the past. Specifically, we aim to answer several research questions that can be tested from detailed fieldwork, ash componentry, and petrographic analyses, as follow; 1) What is the nature of proximal stratigraphy of the Tangkuban Parahu volcano? 2) What was the role of the subvolcanic hydrothermal system in the past? 3) Does magmatic intrusion contribute to a volcanic eruption?

2.2. Terminology

Subvolcanic hydrothermal systems are an active hydrothermal system underneath the volcanic edifice of stratovolcano (Ohba and Kitade, 2005).

Volcanic products are ejected material from all types of volcanic eruptions (i.e., plinian, phreatic, phreatomagmatic). They contain a wide range of type of lithics and pyroclasts (i.e., scoria and pumice).

Volcanic ash is the smallest fragment of the volcanic products (<2 mm in diameter).

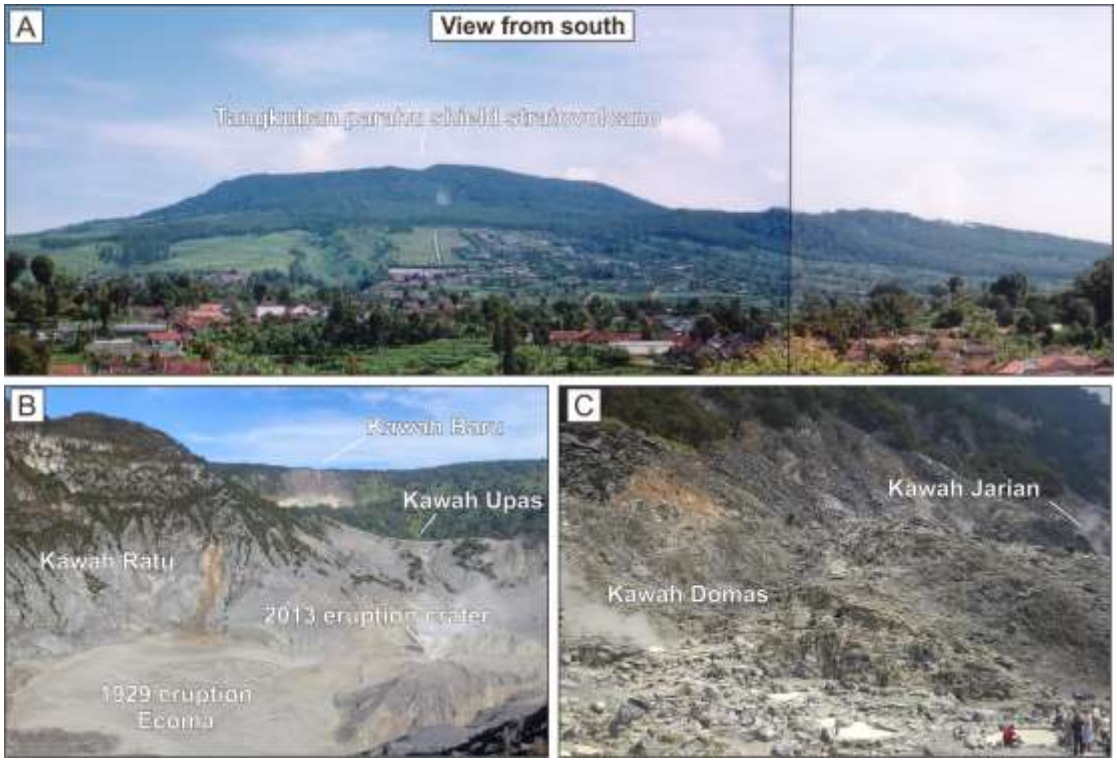

Figure 1. Photographs are showing the Mt. Tangkuban Parahu, Indonesia. A) A shield-like morphology of the stratovolcano (2084 meter above sea level-masl) developed within the prominent arcuate caldera wall of Mt. Sunda. (Photograph from N. Kartadinata). B) The volcano displays an extensive surface manifestation of the active hydrothermal system at several summit craters, C) as well as the parasitic craters (Domas, Jarian) at SE side of the summit. Moreover, most of the proximal deposits were derived from eruptions close to the Ratu crater, similar to the most recent 2013 eruption crater.

2.3. Overview of the Tangkuban Parahu Volcano

The Tangkuban Parahu is a shield-like stratovolcano (Fig. 1A) and a part of the Sunda Volcanic Complex (SVC), which includes the extinct Sunda and Burangrang volcanoes. The volcano develops at the rear volcanic chain of Sunda volcanic arc, as a result of continuous subduction of the Indo-Australia plate below Eurasian Plate with a speed of 6-7 cm/yr (Fig.2A) (Tregoning et al., 1994; Hall, 2002).

The volcanic activity of Mt. Tangkuban Parahu (Fig. 2B) has been divided into three main episodes: 1) pre-Sunda caldera, 2) Sunda caldera, and 3) Tangkuban Parahu (Van Bemmelen, 1949; Kartadinata et al., 2002; Nasution et al., 2004) (Fig. 2C). The onset of the Pre-Sunda Caldera episode is still poorly understood. It began either Gelasian (Van Bemmelen, 1949) or Calabrian of ca. 1.105 Ma (Sunardi and Kimura, 1998). The Pre-Sunda Caldera deposit comprises a series of pyroclastic rocks and lava flows

(Batunyusun lava formation) that unconformably overlie the Neogene sedimentary rocks (Subang Formation) (Fig. 2C). The volcanic activity was terminated at 0.56-0.5 Ma (Sunardi and Kimura 1998), by the emplacement of caldera-forming Cisarua Ignimbrite (Kartadinata, 2005), which was then overlain by the Sunda volcanic group (Sutoyo and Hadisantono, 1992) from the Sunda caldera episode at 0.21-0.1 Ma (Kartadinata, 2005) (Fig. 3C). The volcanic products of Sunda episode comprise a lahar deposit, lava flow, and pyroclastic rocks, including a large volume of Manglayang Ignimbrite deposit. Most of the eruptive products are widely distributed on the south-northeast of the prominent arcuate caldera wall.

The Tangkuban Parahu episode began at 0.09 Ma (Kartadinata et al., 2002). It was mainly characterized by an explosive eruption associated with the magmatic, phreatomagmatic and phreatic activity, as well as the effusive eruption of basaltic lava at 0.04 Ma (Sunardi and Kimura, 1998). The Old Tangkuban Parahu formation comprises 30 tephra layers of pumice and scoria flow, that is associated with accretionary lapilli. These include nine major Plinian eruption periods (Kartadinata et al., 2002), which were assumed to erupt from Upas and Badak craters, although it remains poorly understood. During the Holocene epoch, the volcanic activity is thought to be dominated by phreatic-explosions, which erupted from the separate craters (e.g., Ecoma, Ratu, Siluman, Baru, Jarian) (Fig. 1B and 1C). According to the brief description of Kartadinata et al. (2002), the Holocene volcanic products consist of interbedded sandy to clayey ash, altered ejecta, and base surge deposits.

Furthermore, recent surface expression of the volcano displays a massive hydrothermal activity within the summit craters (e.g., Ratu, Baru, Domas) (Fig 1B and 1C) by the persistence of solfataric and fumarole activity at a temperature of 90-100º C (Suryo, 1981 and 1985).

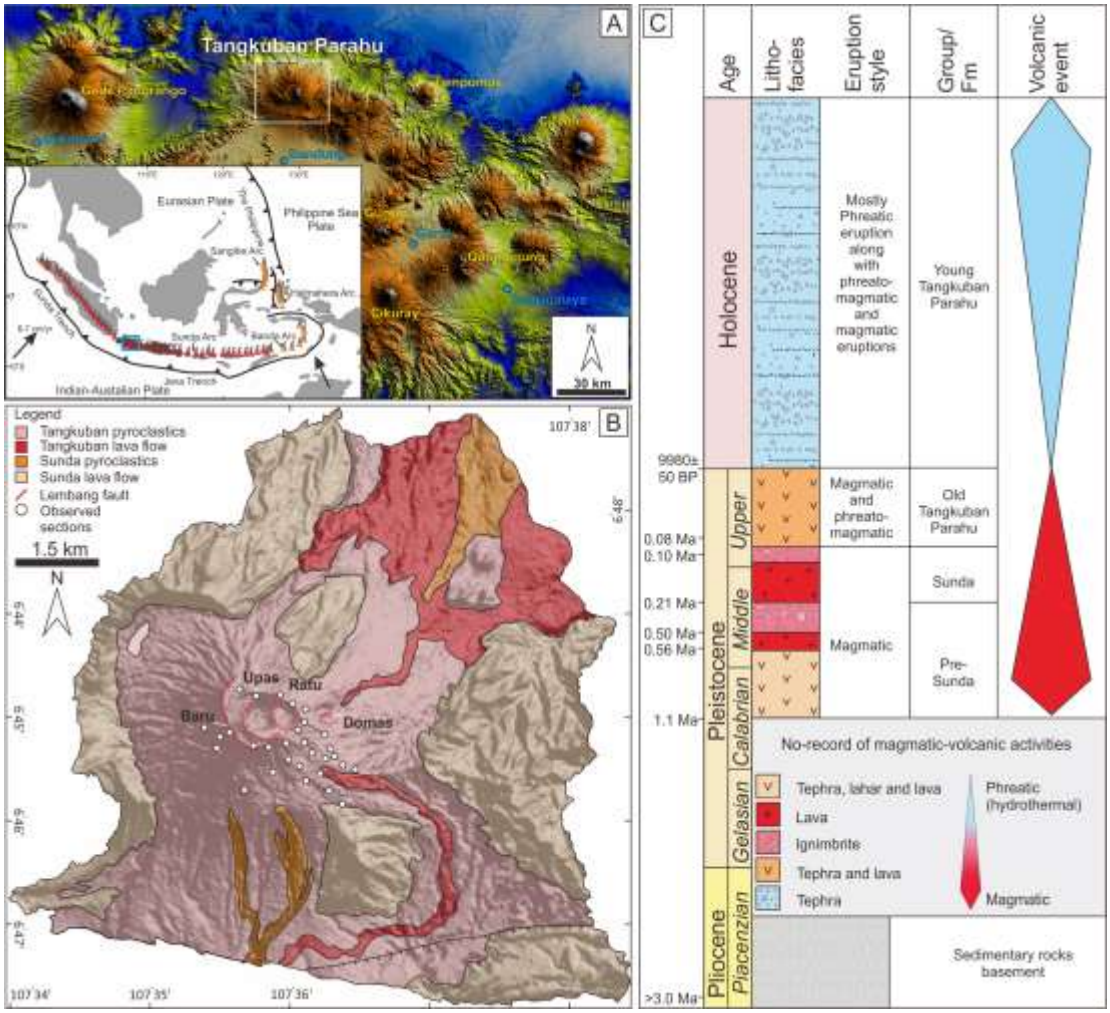

Figure 2. (A) Map shows the location of the Mt. Tangkuban Parahu, Indonesia, within the Sunda volcanic arc. (B) Geological map of the Mt. Tangkuban Parahu. The volcano is covered by a volcanic succession of explosive magmatic and phreatomagmatic eruptions from the Old Tangkuban Parahu Formation, whereas the younger volcanic products extend only ~1 kilometer from the summit. (C) Simplified stratigraphic overview of the studied area. The volcanic succession from the Pre-Sunda and Sunda Caldera episodes are based on a compilation from Bemmelen (1949), Sutoyo and Hadisantono (1992), and, Sunardi and Kimura (1998). The Tangkuban Parahu episode was compiled in conjunction with a brief description of Kartadinata et al. (2002), Kartadinata (2005) and Nasution et al. (2004). Thickness is not to scale. For this study, we focused on the Holocene volcanic activities younger than 10.000 BP.

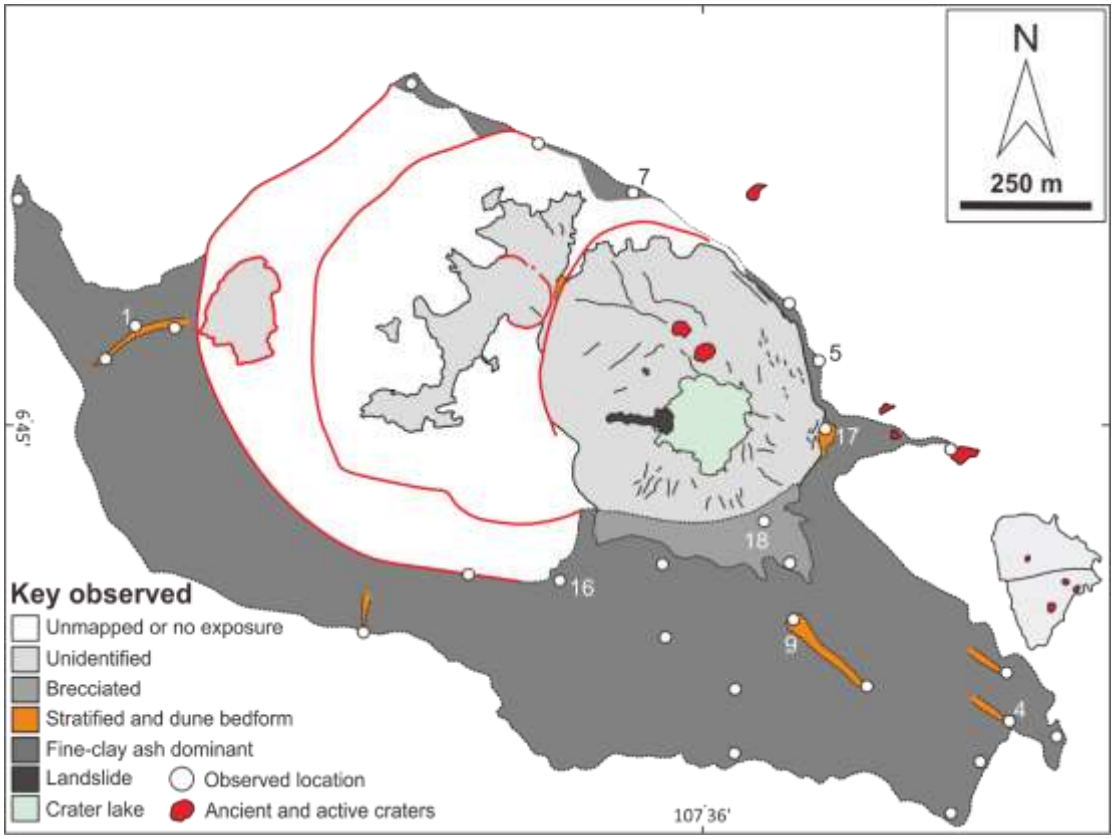

Figure 3. Geological map of the proximal area of Tangkuban Parahu volcano displaying the observed locations and lithological distribution of proximal volcanic products

2.4. Methodology

2.4.1. Fieldwork

Field observation was focusing on macroscopic volcanic facies (e.g., Mcphie et al., 2003), sorting, and grain size to diagnose the emplacement process of the volcanic products (e.g., Cas and Wright 1988). The tephra succession is correlated based on the similarity of characteristics in each tephra layer, together with the presence of unconsolidated very-fine grain layer of paleosols (Miyabuchi, 2015).

2.4.2. Radiocarbon dating

Charred-wood and charcoal were collected from two tephra layers at the crater rim (location 5 and 6) for radiocarbon dating. These are used to provide the absolute age of those selected volcanic products. Both samples were handpicked in the field and placed into an aluminum foil container. Sample treatment of Acid-Alkali-Acid (AAA) and the

measurement of ^{14}C concentration with Accelerator Mass Spectrometer (AMS) were undertaken at Beta Analytic Laboratory. Moreover, the ^{14}C ages were calibrated using IntCal13 (Reimer, 2013).

2.4.3. Sample preparation and analytical techniques

A total of 25 volcanic products were sampled during the fieldwork with 50-100 grams in weight. Samples were entirely hand-sieved under wet condition into different mesh sizes ($-2 \leq \phi \leq 4.5$). Each fraction was bathed with distilled water and cleaned by an ultrasonic cleaner. These steps were repeated several times to clean the finer ash particles from coated clay and dust. Moreover, Cleaned ash fractions were dried with an oven at a temperature of 40 ℃ for 12 hours.

Componentry analysis was carried out to classify the ash component and distinguish the phreatic explosion from the phreatomagmatic eruption based on components, whereas the petrography observation on some thin sections was performed to validate the component determination under a binocular microscope. For componentry analysis, the coarse ($1 \leq \phi \leq 2$) and fine ($3 \leq \phi \leq 4$) ash fractions were observed under a binocular microscope. The component of ash fraction was counted with a total of 1400-2000 grains to provide an adequate ash particle distribution. Volcanic ash was classified into several different types of components, according to their physical appearances (e.g., color, alteration, volcanic texture; Ohba et al., 2007; Suzuki et al., 2013; Pardo et al., 2013; Alvarado et al., 2018).

Petrography of ash particles ($1 \leq \phi \leq 2$ and $3 \leq \phi \leq 4$) was studied using an optical and electron microscopes at the Faculty of International Resource Science, Akita University, with a scanning electron microscope (SEM, JSM-IT300, JEOL) equipped with an energy dispersive spectrometer (EDS, INCA X-act, Oxford Instrument). Microprobe analysis of minerals was carried out with an accelerating voltage of 15kV, a probe current of 2.2 nA, a working distance of 10 mm, and a counting time of 30-80s, using cobalt for the standard.

2.5. Results

2.5.1. Proximal tephra-stratigraphy

In the proximal area, the volcanic succession consists of some mappable tephra units (Fig. 3). Good outcrop exposures are located at the summit crater rim and towards the southern sector of the volcano within the radius of 0.5-1.5 km. For this study, a total of 29 locations (Fig. 3) were observed. These include re-observation of some locations that had been observed by Kartadinata et al. (2002) in the past. The tephra succession has a total thickness of ~4 m for the entire units. The lithologies are composed of fine-clay and coarse ashes, lapilli tuff, and pyroclastic breccia. They mostly show a massive structure, although some of the tephra units display sedimentary structures (i.e., cross stratification, dune bedform). The comparison with the previous work provided in *supplementary I*, whereas composite stratigraphy is shown in Fig. 6.

Unit 1

Unit 1 is the lowest stratigraphic unit in this study, consisting of three tephra layers (layers 1A, 1B, and 1C). Exposure of this unit is limited to loc.1 and loc. 16 with a thickness of ~20 cm (Fig. 4A). Layer 1A is white to yellow fine-clay ash. It almost contains no lithic fragments. Layer 1B is grey coarse ash and 5-10 cm in thickness (Fig. 4A). It displays a linear fabric of glassy fragments on a scale of <1 mm, which is characteristics from other tephra units. Layer 1C is white to brown fine-clay ash. It contains considerably high concentration (>20%) of lithic fragments. Moreover, lithics are wholly composed of angular to rounded altered fragments (<10 cm in diameter).

Unit 2

Unit 2 consists of two tephra layers (layer 2A and 2B) of fine-clay ash, which was observed at loc. 1, 16, and 18. Both layers are different in color, as well as the degree of grain cohesion. Layer 2A shows white to brown with slightly loose fraction due to abundant embedded altered lithic fragments (<1 cm in diameter), whereas the layer 2B displays white in color, dense, and less abundant altered lithic fragments (<5 cm in

diameter). The contact of these layers is obscure and appears as a normal grading structure (loc. 1) (Fig. 4C).

Unit 3

Unit 3 is yellow to red volcanic products, comprising three main tephra layers (3A, 3B, and 3C). Layer 3A is matrix-supported fine-clay ash. This layer contains block-sized altered and vesiculated lava fragments. The size of fragments decreases significantly towards the distal area (loc. 9 to loc. 4). Layer 3B is stratified dark-brown coarse ash, which occurs as a dune bedform along with local planar stratified laminae. Each layer has a thickness of 5-20 cm with a total of ~1 m for entire succession. The deposit is predominantly distributed on the crater rim and significantly decreased in thickness towards the southern sector (10-20 cm in thickness). Layer 3C is yellow fine-clay ash. This layer rarely contains block-sized fragments.

Unit 4

Unit 4 is the thickest unit in the proximal area. It is composed of fine-clay ash, coarse, and lapilli tuff lithologies, which can separate into six tephra layers (loc. 17, and Fig 4D and 4F). Evidence of dormancy is absent from the unit, indicating a single emplacement period with a total thickness of ~1.5 m at the crater rim (loc. 17).

Layer 4A is massive fine-clay ash, which rarely contains lapilli-sized altered fragments. Layer 4B is grey coarse ash and contains charcoal fragments. ^{14}C dating from a charcoal fragment yielded 982-904 cal BP (probability of 90.4%; see in Table 1.). Both layers 4A and 4B are predominantly widespread throughout the southern sector within the radius of ~1 km. Layer 4C is massive white to yellow fine-clay ash. It is characterized by relatively poorly sorting and a slightly loose fraction due to abundant of altered lithics. Layer 4D is composed of an alternation of coarse ash (>5 cm in thickness) and fine-clay ash laminae (Fig. 4F). It hosts lithic blocks (>10 cm in diameter), which makes up 1% proportion for the entire layer. Layer 4E is massive fine-clay ash, which is mostly encrusted by oxidation. Layer 4F is a composite layer of stratified lapilli tuff, which is situated at the uppermost of Unit 4. Lapilli tuff layers display sedimentary structure, such as planar bedding along with local low-angle cross-stratification and the

thickness range from 2 to 8 cm. It is interesting to note that layers 4D and 4F contain scoria fragments (5-15 cm in diameter), which frequently occur as a sag structure and represent the impact of ballistic during the eruption.

Table 1. Summary of radiocarbon dating from charred-wood and charcoal in volcanic products.

Sample ID	Samples	Tephra unit Layer	$\delta^{13}C$ (‰)	Con. ^{14}C age (yr BP)		Cal ^{14}C age
TPCW-01	Carbonized wood	Unit 8 Layer 8A	-26	111.44	0.42 pMC	1993 - 1998 cal AD (89.8%) 1957 - 1958 cal AD (-5.6%)
TPCH-02	Charcoal	Unit 4 Layer 4B	-23.3	1020	30	982 -904 cal BP (90.3%) 856-830 cal BP (4.1%) 809 -803 cal BP (0.3%) 1042-1038 cal BP (0.7%)

Unit 5

Unit 5 consists of two tephra layers (layer 5A and 5B). Lithology is matrix-supported fine-clay ash, which has similar characteristics to Unit 2. This unit is a typical volcanic product in the proximal area (Fig. 4C). Both layers contain lapilli-sized fragments, although they are limited in layer 5A than layer 5B.

Unit 6

Unit 6 comprises three tephra layers (layers 6A, 6B, and 6C). Layer 6A is the fine-clay ash matrix with altered lithics (>1 cm in diameter). It shows a white to yellow in color and structurally massive. Layer 6B is finely-laminated coarse ash. The thickness varies from 5 to 30 cm. Layer 6C is white to yellow pyroclastic breccia.

Unit 7

Unit 7 consists of massive pyroclastic breccia with a thickness of 2-3 m. It is abundant in clasts, up to 40 cm in diameter (Fig 4G, 5A, and 5B). Clasts are heterolithic, consisting of hydrothermally altered, vesiculated lava and rare scoria fragments within a clay-size matrix. The fragment concentration is higher (25-50%) at the base of the deposit, whereas the upper portion of the layer shows a lower fragment proportion (Fig. 5A and 5B).

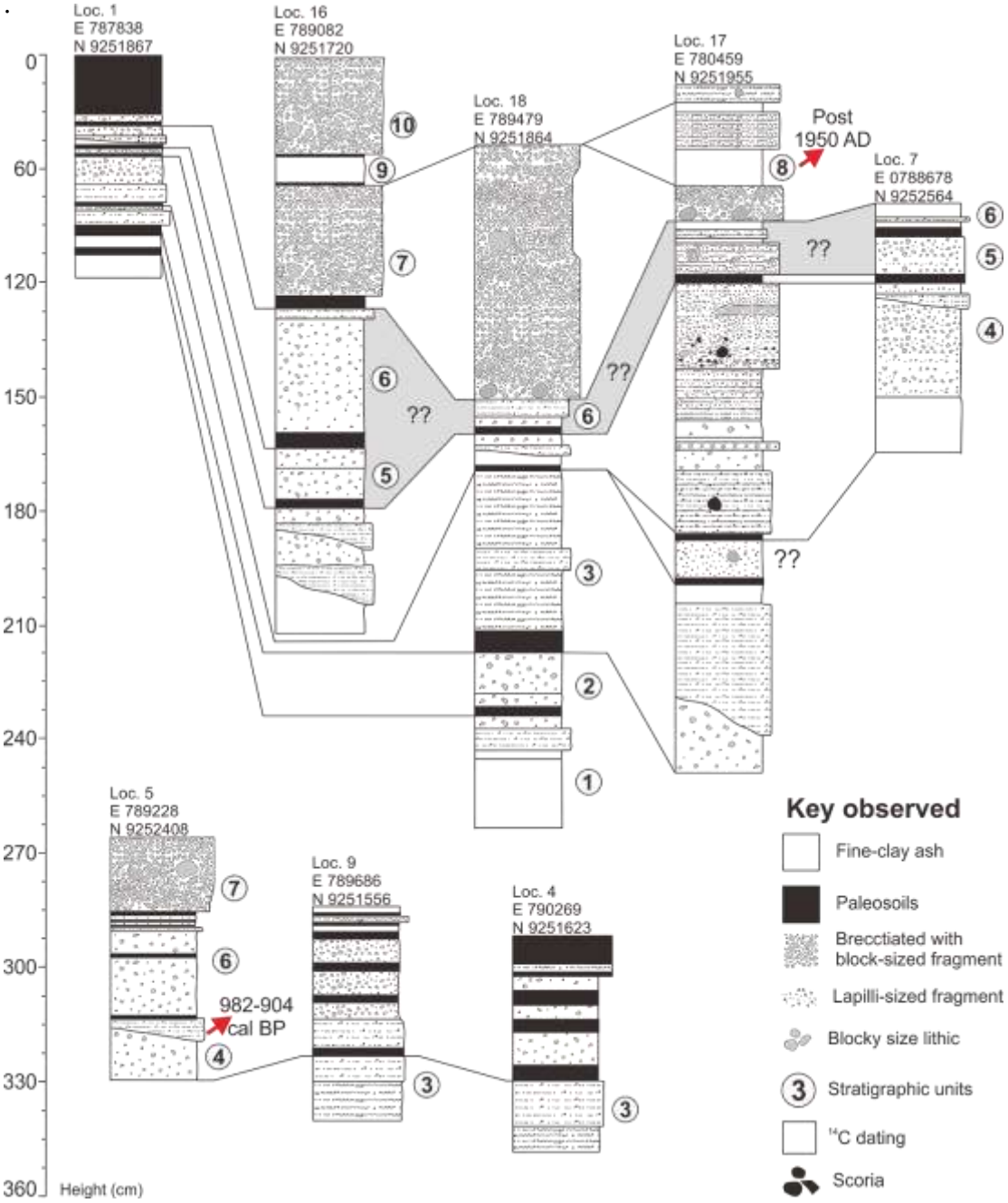

Figure 4. Detailed tephra-stratigraphy and correlation of eight selected sections at the crater rim (Ratu and Upas) and southern flank of the summit crater. Each section exhibits a variety of volcanic units, which is separated by the presence of very thin weathered, loose and organic-rich soil layers. The stratigraphy is divided into 10 tephra units, although there are still several uncorrelated tephra-layers. The units are predominantly composed of fine-clay ash with lapilli-sized fragments, coarse ash, lapilli tuff, and pyroclastic breccia containing hydrothermally altered lithic clasts.

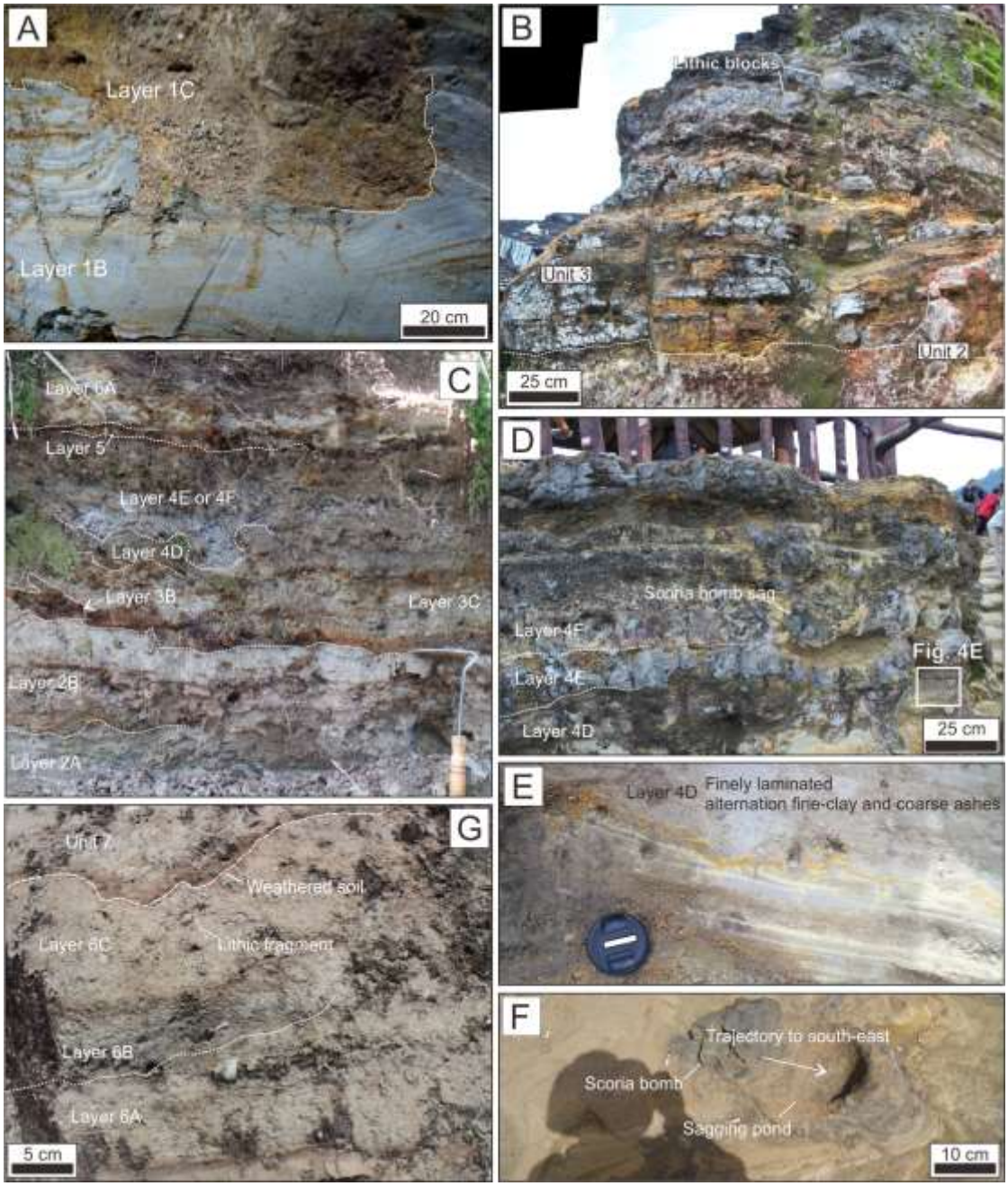

Figure 5. Photographs showing the examples of tephra outcrops in the proximal area. A) Irregular contact between coarse and fine-clay ash in Unit 1 (Layers 1A and 1B), B) as well as in Unit 2 and 3. C) Several tephra layers (Unit 2 to 6) occurs on the western flank. D) Unit 4 is composed of an alternation of coarse ash and fine-clay ash (layer 4D), fine-clay ash (Layer 4E), and stratified coarse ash (layer 4F). E) The detailed photograph displays the fine-clay ash laminae along with coarse ash layers (Layer 4D), F) which includes sag structure of scoria in Unit 4. G) Coarse ash occurs as a lenticular structure in between of fine-clay ash of Unit 6.

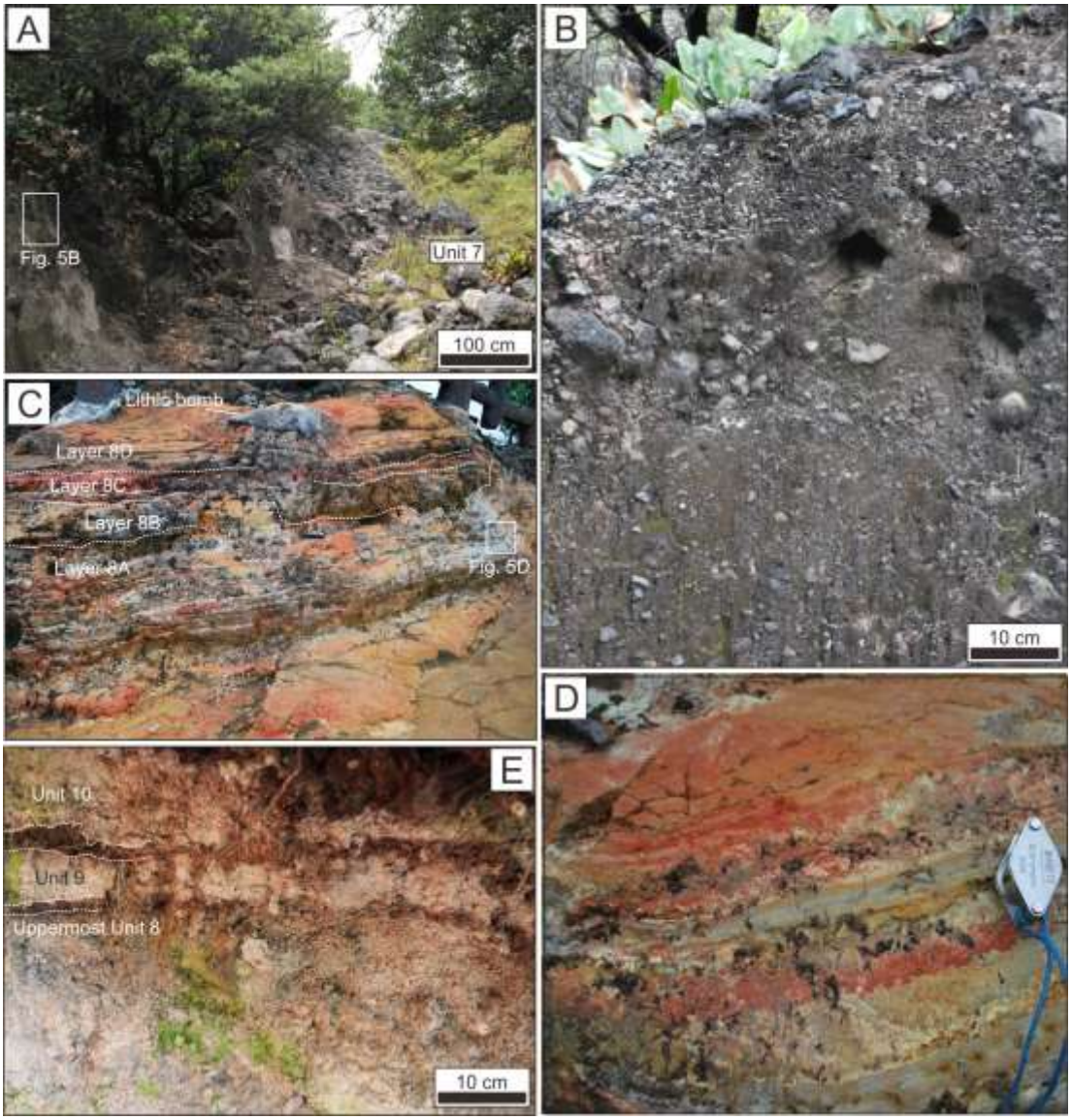

Figure 6. Continued from Fig. 5. A) Photograph showing the pyroclastic breccia of Unit 7. B) In Unit 7, clasts are abundant and heterolithic, which mainly concentrated at the top and base of Unit 7. C) photograph shows the tephra layer of Unit 8, consisting of fine-clay ash and lapilli tuff. D) detailed photograph shows a laminated structure of fine-clay ash in Layer 8A. E) Unit 8 to 10 are separated by very thin paleosols (1-3 cm in thickness).

Unit 6

Unit 6 comprises three tephra layers (layers 6A, 6B, and 6C). Layer 6A is the fine-clay ash matrix with altered lithics (>1 cm in diameter). It shows a white to yellow in color and structurally massive. Layer 6B is finely-laminated coarse ash. The thickness varies from 5 to 30 cm. Layer 6C is white to yellow pyroclastic breccia.

Unit 8

Unit 8 consists of four tephra layers (layers 8A, 8B, 8C, and 8D). The lithology is an alternation of fine-clay ash and lapilli tuff (Fig 5C and 5D). All layers occur as a local mantle bedding at loc. 18 with 10 to 30 cm in thickness. Layer 8A is finely-laminated (<1 cm in thickness) fine clay ash with white to red color (Fig. C and D). Layer 8B is yellow to brown lapilli tuff, which appears as a lenticular structure between layers 8A and 8B. The charred-wood from layer 8B yielded 111±0.42 pMC of modern carbon concentration, which corresponded to calibrated age of post-1950 AD. Layer 8C comprises laminated fine clay ash, whereas the layer 8D is lapilli tuff, containing subangular-shape altered lithics.

Unit 9

Unit 9 is massive fine-clay ash (Fig. 5E). This layer was observed only at loc. 16, which is situated in-between recognizable brownish paleosols. Unit 9 has a thickness of ~10 cm at the loc. 16.

Unit 10

Unit 10 is the youngest volcanic unit observed in this study. The lithology is massive white to grey pyroclastic breccia. Thickness ranges from 0.5 to 1 m (Fig. 5E). It is predominantly distributed only at the summit, which is similar to Unit 7 and Unit 9. It is clast supported and wholly composed of hydrothermally altered lithic fragments with fine-clay ash as a matrix. The lithic fragments vary in size (10-20 cm in diameter), showing an angular to subrounded clasts shape.

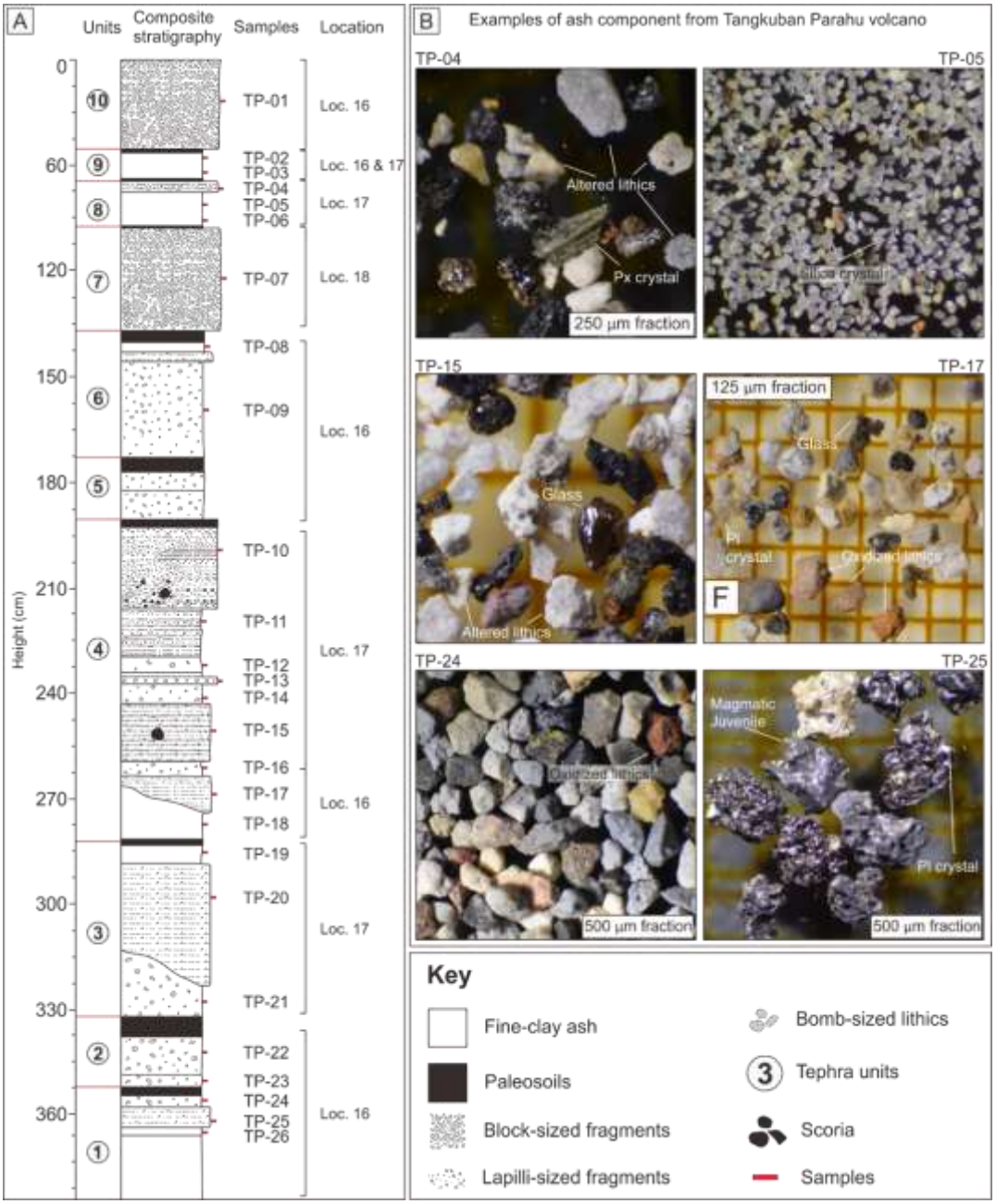

Figure 7. A) Composite tephra-stratigraphy of proximal deposits from three sections (loc. 16, 17 and 18), including sampled horizons of the 27 samples. B) Photographs are showing the examples of volcanic ash from the volcanic product, comprising hydrothermally altered lithics, coherent crystalline lithics (e.g., lava, hypabyssal rocks), oxidized lithics, free crystal (e.g., quartz, pyroxene, quartz), and magmatic juvenile (e.g., scoria, glass). All components are observed under the binocular microscope based on physical appearances (e.g., Ohba et al., 2007; Suzuki et al., 2013).

Table 2. Summary of componentry analysis from 25 volcanic products.

Sample ID	Tephra unit	Lithologies	Hydrothermally altered		Coherent crystalline		Magmatic juvenile	Oxidised	Free crystal	Total counting
			White	Yellow	Phyric	Aphyric				
TP-01	Unit 10	Pyroclastic breccia	809	348	9	311	0	119	243	1839
TP-02	Unit 9	Fine-clay ash	150	179	6	44	0	174	1280	1833
TP-04	Unit 8	Lapilli tuff	1200	662	3	87	45	10	78	2085
TP-05		Fine-clay ash	347	202	8	42	0	267	889	1755
TP-06		Fine-clay ash	336	10	9	3	18	786	320	1482
TP-07	Unit 7	Pyroclastic breccia	757	1107	0	18	30	22	24	1958
TP-09	Unit 6	Fine-clay ash	708	674	12	288	60	100	40	1882
TP-10	Unit 4	Lapilli tuff	760	237	35	195	714	0	320	2261
TP-11		Lapilli tuff	358	402	10	347	650	79	130	1976
TP-12		Fine-clay ash	730	296	8	254	780	64	96	2228
TP-13		Lapilli tuff	1034	446	10	110	380	37	80	2097
TP-14		Fine-clay ash	760	237	35	195	714	0	320	2261
TP-15		Coarse ash	800	208	10	220	572	46	76	1932
TP-16		Fine-clay ash	659	311	14	60	714	98	320	2176
TP-17		Coarse ash	407	402	14	116	609	80	145	1773
TP-18		Fine-clay ash	810	768	15	104	44	212	38	1991
TP-19	Unit 3	Fine-clay ash	708	674	12	288	60	100	40	1882
TP-20		Coarse ash	934	664	12	95	170	10	80	1965
TP-21		Fine-clay ash	1020	760	2	28	20	198	98	2126
TP-22	Unit 2	Fine-clay ash	1200	662	3	87	45	10	78	2085
TP-23		Fine-clay ash	765	929	4	264	0	94	22	2078
TP-24	Unit 1	Fine-clay ash	869	817	17	185	0	58	54	2000
TP-25		Coarse ash	587	173	6	351	650	79	130	1976
TP-26		Fine-clay ash	530	689	2	105	567	81	172	2146
TP-27		Fine-clay ash	902	476	16	330	67	143	69	2003

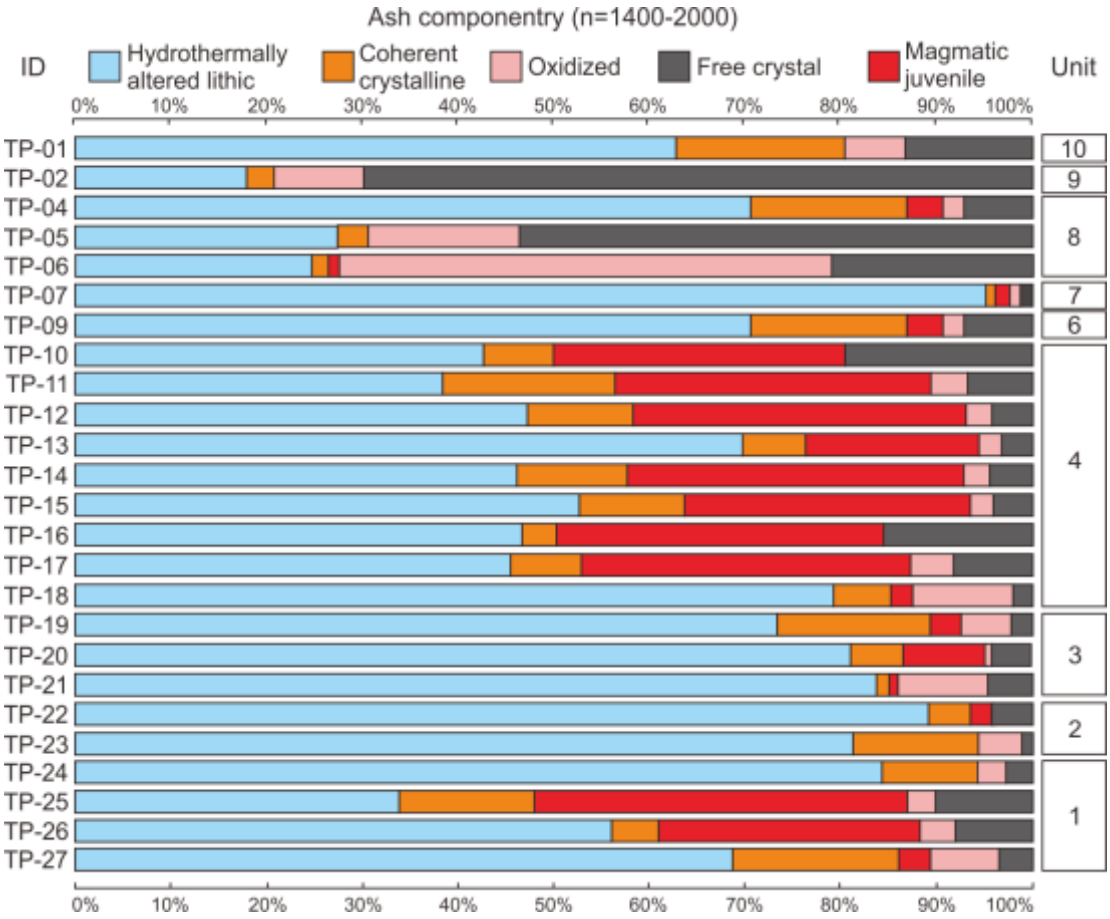

Figure 8. Diagram showing the results of componentry analysis with the total n=1400-2000 ash particles.

2.5.2. Componentry analysis

Componentry classification

The schematic section with sampling horizons and microscopic binocular photographs of the ash particles are shown in Fig. 6. Ash particles were divided into five type components; 1) hydrothermally altered lithics, 2) oxidized lithics, 3) coherent crystalline lithics, 4) magmatic juvenile, and 5) free crystal. Ash components are further described based on characteristics from binocular microscope observation.

1. Hydrothermally altered lithics are present as white and yellow blocky fragments. They mostly appear with vitreous and earthy luster, respectively.
2. Oxidized lithics are coated by brown to red stain (i.e., coherent crystalline; magmatic glass).

3. Coherent crystalline lithics display coherent rock textures (i.e., phyric; aphyric) with earthy luster. They are possibly derived from several types of coherent rock (i.e., extrusive and intrusive rocks).
4. Magmatic juvenile displays a vitreous luster with green and black color, consisting of vesiculated and dense glass particles. This component occurs as subangular-angular fragments and smooth surface of the glass, together with substantially low vesicle textures (Fig. 6, TP-15 and TP-25).
5. Free crystals are isolated minerals. For instance, the pyroxene grains appear as greenish orthorhombic crystal morphology, whereas plagioclase grains occurs as transparent and prismatic crystal. Quartz is present as a subangular to subrounded, equant, and transparent crystals.

Componentry distribution

The distribution of ash component from the analyzed samples are shown in Table. 2 and Fig. 7. All samples contain the five components (i.e., hydrothermally altered lithics, oxidized lithics, coherent crystalline lithics, magmatic juveniles, and free crystals). The components in the samples vary significantly in proportion. This proportion clearly reflects a complex fragmentation process during the eruptive events. In the samples, hydrothermally altered lithics are present within all samples and have a broad range of proportion (18%-93%) compare to the other components. The coherent crystalline lithics show a rather small proportion (<20%), although the components present in all analyzed samples. Oxidized and free crystal components generally display low proportions (<20%) in Unit 1 to 7. However, their abundance shows anomalies in Unit 8 and Unit 10, which exceeds to higher percentages (>25%). Lastly, the presence of magmatic juvenile is fluctuative, ranging from 5% to 40 % in proportion. The magmatic juvenile prominently displays a higher proportion in some samples from Unit 1, Unit 4, and Unit 6; whereas in other units their proportions are less (>5%).

2.5.3. Ash petrography: magmatic and hydrothermal minerals

We carried out petrographic observation of the ash to specify the mineralogy, focusing on two mineral groups: 1) magmatic minerals and 2) hydrothermal minerals. More detailed

mineralogy and petrography of the ash particles will be published in a separate article, exclusively for the hydrothermally altered lithics.

Magmatic minerals mostly occur in magmatic juvenile, coherent crystalline, and free crystal components. The magmatic juvenile comprises glassy groundmass and microlite crystals together with vesiculation textures, whereas coherent crystalline components show a volcanic rock texture of porphyritic to pilotaxitic (Fig. 9C and 9D). Magmatic minerals in magmatic juvenile and coherent crystalline lithics mostly share similar mineral assemblages. It comprises quartz, plagioclase, augite, ilmenite, rutile**,** and pigeonite (Fig. 9A, 9C, and 9D). Even though, some of the analyzed coherent crystalline lithics have sanidine occurring in interstitial of quartz as the dominant mineralogical assemblages. They also contain xenocrystic subhedral-euhedral biotite crystals (>50 µm) together with euhedral plagioclase and quartz crystals (Fig. 9D). Quartz crystals in the coherent crystalline components are an igneous origin (Fig. 9B), which is characterized by euhedral and equant shape, containing single-phase inclusion of melt or glass (Fig. 9F).

Hydrothermal minerals are composed of an association of silica (possibly quartz), alunite, and kaolinite, together with accessory minerals of TiO_2 and pyrite. Association of silica and alunite are abundant (Fig. 8E). Some of the silica minerals were determined by using an optical microscope as a quartz crystal. Here, quartz crystals are the hydrothermal origin, which shows a mosaic-texture (Fig. 8F), consisting of interlocked euhedral-equant shape quartz crystals (<10 µm in diameter). Alunite crystals occur as euhedral to subhedral, and equant to elongated lath (5-20 µm in length) crystals along with oscillatory zoning texture suggested from BSE image. Pristine kaolinite mostly occurs as very-fine crystal (<1 µm) and commonly mixed with silica minerals. Accessory minerals are mostly anhedral (<5 µm in diameter) and disseminating on the surface of quartz-dominated ash particles.

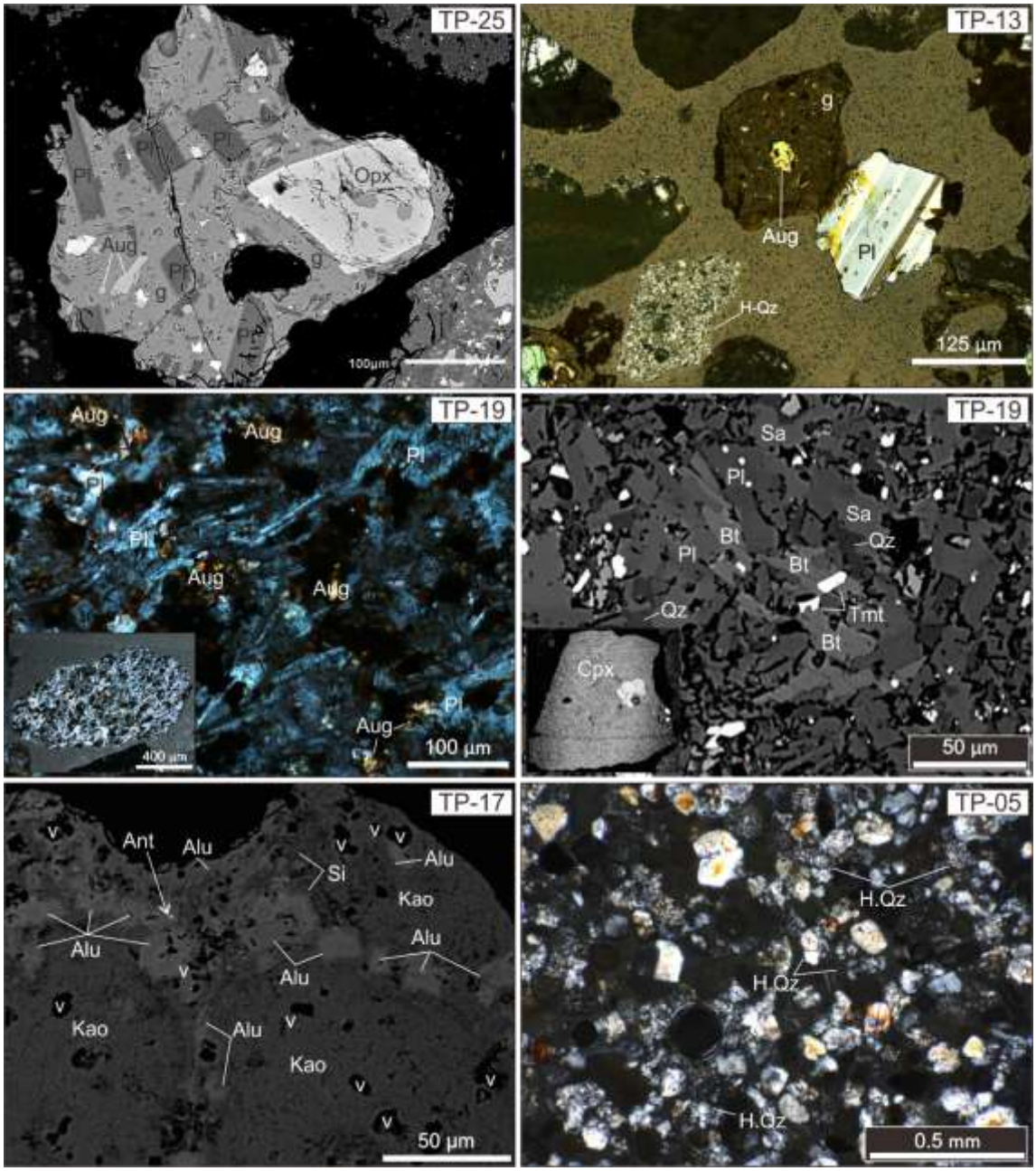

Figure 9. Photomicrograph and backscattered images showing the petrography of ash fractions. A) A BSE image is showing the magmatic juvenile fragment with vesicular texture, consisting of orthopyroxene bearing glass inclusion, plagioclase, augite and ilmenite within the andesitic glass. B) Magmatic juvenile fragments are predominantly present accompanying the mosaic-hydrothermal quartz. C) The pilotaxitic texture of coherent crystalline lithics consists of lath-shaped plagioclase, subhedral-euhedral augite, and ilmenite. D) A BSE image is showing the porphyritic texture of coherent crystalline lithics, consisting of plagioclase, quartz, clinopyroxene, and xenocryst of biotite. E) Hydrothermally altered lithics are predominantly comprised of silica, alunite, kaolinite, and anatase. F) Coexistence magmatic-quartz with mosaic-hydrothermal quartz from the TP-05 sample, the free-crystal rich tephra layers. Abbreviation; *Aug:* augite, *Alu:* alunite, *Bt:* biotite, *Cpx:* clinopyroxene, *Kao*; kaolinite, *M-Qzt*: magmatic-quartz, *H-Qzt:* hydrothermal-quartz, *Pl* plagioclase, *Si:* silica (unidentified polymorph).

2.6. Discussion

2.6.1. Nature of proximal tephra-stratigraphy

The vast majority of volcanic successions at the proximal area of Tangkuban Parahu volcano consists of an alternation of fine-clay and coarse ashes, lapilli tuff, and pyroclastic breccia. Massive fine-clay ash appears to be dominant in all volcanic products. In some units, the fine-clay ash alternated with coarse ash. They predominantly show the irregular contact together with finely-laminated structure, wherein some locations show as lenticular structures. Their emplacement is mostly associated with the lapilli to block-sized lithic fragments (e.g., pyroclastic breccia; upper composite stratigraphy). Their concentration decreases toward to distal area (<1.5 km) (i.e., Unit 2, Unit 3), which is very common for the volcanic products from the low-explosive intensity (e.g., Maeno et al., 2016; Oikawa, 2018). However, it is still challenging to understand their emplacement process (e.g., fall-out, flow) due to the limited observed locations and mostly closed the sourced-vent (Ratu crater). Unit 3 and Unit 4 show very distinct sedimentary structures. Unit 3 display a prominent dune-bedform structure at the crater rim, whereas Unit 4 displays a planar and low-angle cross-stratification of lapilli tuff. Both units indicate that they were emplaced as a pyroclastic base surge. In Unit 4, sagging structure by scoria fragments suggests that the volcanic product was deposited under wet-condition (Cas and Wright, 1987).

Overall, the nature of proximal volcanic succession suggests that the past eruptions are predominantly composed of an intensive explosive eruption, which is associated with phreatic and phreatomagmatic events. These results are mostly consistent with the previous observation at Tangkuban Parahu volcano (Kartadinata et al., 2002).

2.6.2. Role of the hydrothermal system

Hydrothermally altered lithics are present in all volcanic products, which were suggested from componentry analysis. It indicated that the hydrothermal system has been very active in the pre-historical time. From petrography, the hydrothermally altered fragments contain silica and alunite as a dominant hydrothermal mineral, indicating advanced argillic alteration is (Arribas, 1995; Hedequist and Taran, 2013) extensively present at the crater-

conduit. This is similar to surface hydrothermal zonation at active craters (Syahidan et al., 2005). Silica (quartz), alunite, and kaolinite are precipitated from acidic vapor (e.g., SO_2/H_2; HCL/NaCl) under a low-pressure condition, which encountered the country rock and produced extreme alteration effectively by hydrolysis reaction. The process reflects a range of formation temperature from 100 to 300 ℃ (Arribas, 1995), which present near-surface and surface of mature stratovolcano edifice (e.g., Hedenquist and Taran, 2013).

Advanced argillic alteration is predominantly accompanied by an enormous amount of residual silica precipitation (Hedenquist and White, 1992). One of the most notable observations on components (Fig. 7) is that hydrothermally altered lithics are abundant in Unit 1 to 7, whereas they partly replaced by abundant free crystals of hydrothermal quartz in Unit 8 and 10. This observation indicates extensive silicification at the crater conduit before the eruptions, which provides a capacity to cap or isolate the steam or gasses produced by the hydrothermal activity. If build-pressure of hydrothermal fluid overcomes the yield strength of the caprock, failure of overburden rock leads to the sudden decompression, which results in an explosive phreatic eruption. Therefore, the volcanic products contain abundant fragments derived from the caprock (e.g., silicified rock).

2.6.3. Magmatic contribution

The magmatic juvenile is observed from the componentry analysis. Cashman and Hobblit (2011) suggested that even a small proportion of magmatic juvenile can indicate the presence of a shallow intrusion. Therefore, the contribution of magmatic intrusion should also be considered for the volcanic eruptions of studied tephra stratigraphy. The magmatic juvenile is considerably present in many samples and shows a prominent proportion in Unit 1 and Unit 4. This indicates the periodic introduction of magmatic intrusion to the shallow volcanic edifices. The hydrothermally altered lithics also occur together with the magmatic juvenile, indicating fragmentation of altered country rocks during the volcanic eruption. Most of the magmatic juvenile fragments mostly are present as a dense fragment together with a smooth glass surface, suggesting magma-water interaction (Heiken and Wohletz,1985). Moreover, the presence of vesiculation texture on the magmatic juvenile indicates volatile release, which happens during the ascent of magmatic intrusion (e.g., Alvarado et al., 2015) and is also responsible for the overpressurized condition at the

crater-conduit due to vapor plume expansion below the crater (e.g., Henley and Berger, 2011).

2.7. Conclusion

This study presented the field observations on the proximal tephra stratigraphy, componentry analysis and petrography of volcanic product from Mt. Tangkuban Parahu. The following are concluded based on the observation;

1. Volcanic products at proximal area consist of 10 tephra units, comprising fine-clay and coarse ash, lapilli tuff, and pyroclastic breccia. Their presence indicates the intense explosive eruption in the past, which is mostly distributed close to the summit craters.
2. The volcanic products are composed of hydrothermally altered lithics, oxidized lithics, coherent crystalline lithics, magmatic juvenile, and free crystal, indicating a complex process during the eruption process, involving fragmentation of country rock (hydrothermally altered zonation) and contribution of magmatic intrusions.
3. The hydrothermal fluid affects the system of crater-conduit and precipitates silica or quartz, alunite, and kaolinite. Abundant silicified lithics and quartz crystals imply a significant role of silicified cap rock before sudden decompression of hydrothermal fluid.
4. The presence of magmatic juvenile in many tephra layers indicates the periodic introduction of magmatic intrusion into the shallow of volcanic edifices. The intrusion might have changed the condition of the hydrothermal system due to degassing from magma, resulting in vapor plume expansion.

5. The phreatic explosion appears to be a dominant eruption type for the entire volcanic products at the proximal area, although a few pulses of phreatomagmatic eruptions also observed from field and componentry observation, which is recorded from unit 1 and 4 (ca. 982-904 cal BP).

Chapter 3
Exploring the hydrothermally altered lithics: mineralogical and sulfur isotopic studies of proximal volcanic product at Tangkuban Parahu volcano, Indonesia.

3.1. Introduction

Phreatic (hydrothermal) and phreatomagmatic eruptions are common volcanic events in the subduction-related volcanoes (Wohletz and Heiken, 1992; Brownee and Lawless, 2002). Both eruptions have relatively mild explosivity (VEI 1- VEI 3), but it can lead to the severe proximal hazard (Breard et al., 2014; Fitzgerald et al., 2014). The phreatic eruption is associated with seismic shock (Yamomoto et al., 1999) induced catastrophic failure of overburden rock in the crater conduit, which followed by sudden decompression hydrothermal fluid (Ohba et al., 2007, Oikawa et al., 2018). On the other hand, the phreatomagmatic eruption is predominantly related to magma-water interaction at a depth of volcanic edifices (Wohletz and Heiken, 1992) and commonly also associated with the interaction of magmatic intrusion with a hydrothermal system, so-called magmatic-hydrothermal eruption (Brownee and Lawless, 2002). Both eruptions commonly termed as hydro-volcanic eruption (Ohba and Kitade, 2005). One of the beauties from both eruptions is that the eruption ejected lithic fragments, which were altered in composition caused by circulated hydrothermal fluid below the crater (Ohba and Kitade 2005, Mazot et al., 2008, Minami et al., 2016). Their presence provides an opportunity to understand the temporal change of sub-volcanic hydrothermal system condition within the crater-conduit (Ohba and Kitade 2005; Minami et al., 2016; Imura et al., 2018), which is commonly difficult to characterize from the pattern of surface alteration.

Tangkuban Parahu volcano is one the active volcano in West Java, Indonesia. Tangkuban Parahu hydrothermal system is characterized by fumarolic and solfataric vents at the summit craters (Domas, Ratu, Baru), as well as hot springs and steam-heated pools within the volcano vicinity (Ciater, Batugede, Kancah, Maribaya) (Nasution et al., 2004, Saputra and Suryantini, 2015). To date, these phenomena were accompanied by episodes vertical ground displacement (in 1982, 1986) at the summit, which commonly followed by volcanic eruptions (i.e., 1983 phreatic eruptions) (Dvorak, 1990; CVGHM, 2016). Most

of the previous studies mostly focused on the geochemistry of fumaroles and water from the active craters (e.g., Nasution et al., 2004; Saputra and Suryantini; 2015) with little mineralogical information. The available mineralogical documentation (e.g., Syahidan et al., 2016) only provides a partial view of its enigmatic hydrothermal system at the surface of active craters. In this context, many aspects are still understudied to understand the condition of the subvolcanic hydrothermal system, specifically from the proximal volcanic products.

In this chapter, the focus was given in petrographic observation of ash particles from selected volcanic products with 125 µm, 250 µm, and 500 µm in diameters, including their mineralogical and textural variation within a single ash particle. The hydrothermal mineral assemblages and overprinting relationship (e.g., veinlets, alteration type) were described based on our understanding of the fossil or active geothermal system worldwide (e.g., Hedenquist and Henley, 1987; Arribas, 1995; Sillitoe, 2010; Hedenquist and Taran, 2013), where the hydrothermal assemblages commonly occurs as zonation of hydrothermal minerals beneath volcanic edifice of subduction-related stratovolcanoes (e.g., Kusakabe et al., 1984; Minami et al., 2016). For instance, the advanced argillic alteration is mainly consisting of quartz, alunite, and kaolinite (e.g., Arribas, 1995; Hedequist and Taran, 2013). Additionally, the sulfur isotope is used to constrain the formation of sulfate and sulfide minerals. The results are to address several questions, as follows; What is the hydrothermal alteration style at the crater-conduit? How is the hydrothermal alteration zonation developed at the crater conduit? What is the implication for a phreatic eruption?

3.2. Tangkuban Parahu

Tangkuban Parahu volcano is a 2080 masl (meter above sea level) basaltic-andesite stratovolcano and a part of Sunda Volcanic Complex (Bemellen, 1949; Sutoyo and Hadisantono, 1992) (Fig. 1A). The volcano had been very active in the past ten years (2013 eruptions). The volcano hosts many extinct craters (Putih, Badak, Upas) and active craters (Ratu, Baru, Domas) (CVGHM, 2016) (Fig. 1B). However, the presence of craters is still poorly understood, whether it was formed by phreatic, phreatomagmatic, and magmatic activities.

The pre-historical volcanic activities are mainly composed of explosive eruptions (Kartadinata et al., 2002; Kartadinata 2005) (magmatic, phreatomagmatic, and phreatic eruptions) together with several effusive eruptions (Sutoyo and Hadisantono, 1990). Sunardi and Kimura (1998) reported that the maximum age from basaltic lava flows c.a. 0.18 Ma, which marked the earliest construction of Tangkuban Parahu volcanic edifice (Bemmelen, 1949). Tangkuban parahu volcanic products are composed of typical of subducted-stratovolcano volcanic rocks, range from basaltic to andesitic affinity (Sjarifudin et al., 1984). Sunardi and Kimura (1998) show that volcanic rock consists of two types volcanic suites of calc-alkaline and tholeiitic in composition. Mineralogical observation from lava flows revealed magma mixing and mingling processes (Sunardi and Kimura, 1998). However, petrological studies of volcanic products are still very limited in Tangkuban Parahu (e.g., Sriwana, 1985); thus, the composition of volcanic products relatively remains poorly understood.

Furthermore, Holocene volcanic products are still understudied, in the sense of the eruption process as well as the petrological characteristics of volcanic products. The eruptive product comprises fine and coarse ashes interbedded with base surge deposits. Volcanic product components consist of hydrothermally altered lithics, coherent crystalline lithics, oxidized lithics, magmatic juveniles, and free isolated crystals. It was assumed that the volcanic activity is composed of a series of the phreatic eruption (Kartadina et al., 2002).

3.2.1. Hydrothermal system

Recent surface expression of Tangkuban Parahu volcano consists of active fumaroles and solfataras (Ratu, Baru, Domas) with a temperature of 90-100 ℃ (Sriwarna, 1984; Saputra and Suryantini, 2015). In the past, the temperature of fumaroles was recorded higher than 300 ℃ in 1952, 1961, and 1969 (Suryo, 1981 and 1985). Surface hydrothermal alteration (Fig. 2B) consists of silica dominated alteration (cristobalite and tridymite) together with pyrite and sulfur (Syahidan et al., 2015), which covered the area of ~20.000 m^2 (Fig. 1B; photograph of active crater Fig. 1C and 1D) at the summit of the volcano. A series of phreatic events in 1929, 1961, 1969, 1971, 1983, 1986, 1992, 2004, and 2013 (Kusumadinata, 1976) are also proved the potential role of the hydrothermal system in

producing and capping flashing water or steam gases below the active craters, in this case, Ratu, Domas, and Baru.

3.3. Samples preparation and analytical methods

In this study, volcanic products from phreatomagmatic and phreatic eruptions were used to understand the temporal changing of mineralogical variation in hydrothermally altered lithics. Samples were collected from the volcanic products at the proximal area of Tangkuban Parahu volcano, which was deposited by a series of explosive eruptions during the Holocene epoch (Kartadinata et al., 2002). These eruptive products then divided into ten tephra units with a total of 29 tephra layers (see Chapter 1; Fig. 3.2.). Lithologies are fine-clay and coarse ashes, together with lapilli tuff and pyroclastic breccia. Volcanic products have covered an area of approximately ~2.25 km^2 in close proximity to summit craters. The outcrop is mostly located along the rim of Ratu crater (Fig. 3.1), which thought to be the sourced crater for the studied volcanic products (Kartadinata et al., 2002; Angkasa et al., 2019).

From the outcrop, volcanic products were carefully sampled in the field, by a small shovel and placed to a plastic container. A total of 26 samples (Fig. 3.2) was manually sieved into different mesh sizes ($-2 \leq \phi \leq 4.5$). Each sieved fraction was washed and cleaned by using an ultrasonic cleaner to remove coated clay and dust from the ash particles. Afterward, all samples ($1 \leq \phi \leq 2$ and $3 \leq \phi \leq 4$) were again bathed with distilled water for a maximum of three consecutive times and dried with an oven at 40 ºC for 12 hours.

3.3.1. Mineralogy and textural observations

The ash mineralogy was determined by XRD using a Rigaku Multi-Flex instrument operated at 30 kV and 16 mA, using Cu target anode as a Kα radiation sourced, at Faculty International Resouce Science, Akita University. A total of 21 samples ($1 \leq \phi \leq 2$ and $3 \leq \phi \leq 4$) were ground to a fine powder by iron and agathe mortars. The fine powder was used to produce randomly oriented (bulk) and oriented samples (clay elutriation). Moreover, ethylene glycol treatment was optionally applied to some of the oriented samples to verify the presence of clay minerals (i.e., 14-10 Å mineral groups). Randomly oriented samples were scanned with a step width of 0.01° and a counting time of 1° min^{-}

[1], whereas the oriented samples were scanned with a step width of 0.02° and a counting time of 0.5° min^{-1}. Synthetic quartz was employed as a standard. Mineral intensities are presented as the percentage ratio of measured and quartz standard intensities.

A total of 15 thin and polished section from different ash layers (Fig. 3.2) was studied by optical and electron microscopes at Faculty International Resource Science, Akita University, using a Nikon ECLIPSE LV100N and JSM-IT300 scanning electron microscope (SEM) equipped with energy dispersive spectrometer (EDS, Inca X-act, Oxford instrument). Microprobe analysis was operated at an accelerating voltage of 15 kV, a beam current 20 nA, and a working distance 10 mm. Cobalt was employed as a standard. In order to avoid sample damage, dwell time is different for each mineral. Alunite and kaolinite crystals were analyzed at a dwell time of 30 s, whereas silica (i.e., quartz) and magmatic minerals (i.e., plagioclase, clinopyroxene) were bombarded by the electron beam about 80 s.

In the polished section, the minerals were determined based on their general chemical formulas. For instance, plagioclase-feldspar and clinopyroxene were determined by general mineral formula $A_1T_2Si_2O_8$ and $M1_1M2_1T_2O_6$, respectively, because backscattered electron images are inadequate to judge each mineral phases (Tadeucci et al., 2004). This approach is also applied to hydrothermal minerals (i.e., alunite; kaolinite; quartz). Alunite ($(K,Na,Ca)Al_3(SO_4)_2(OH)_6$) and kaolinite ($Al_2Si_2O_5(OH)_4$) were evaluated by the general formula of $DG_3(TX_4)_2X_6$ (Bayliss et al., 2010) and $X_4Z_4O_{10}(OH)_8$ with a total oxygen number of 11 and 7, respectively. Moreover, Al/Si concentration from EDS detector (~1 ratio) was checked to validate pristine kaolinite crystals from complex intergrowth texture with silica minerals (Minami et al., 2016).

Furthermore, Silica minerals mostly cannot be classified by mineral chemistry from SEM-EDS, except for pristine quartz crystal (SiO_2; 98-100 wt. %). For other silica minerals (e.g., cristobalite, opal), they were determined by Raman spectroscopy, using a Renishaw Invia Raman Microspectrometer operated at a laser power of 150 mW and a spot size 1 µm, and an argon excitation laser of 532 nm. Silica standard was employed to calibrate the Raman peak. A CrystalSleuth software (Laetsch and Down, 2006) was employed to compare the Raman spectra with a specific crystal reference (www.rruff.info; American mineralogist crystal structure databases).

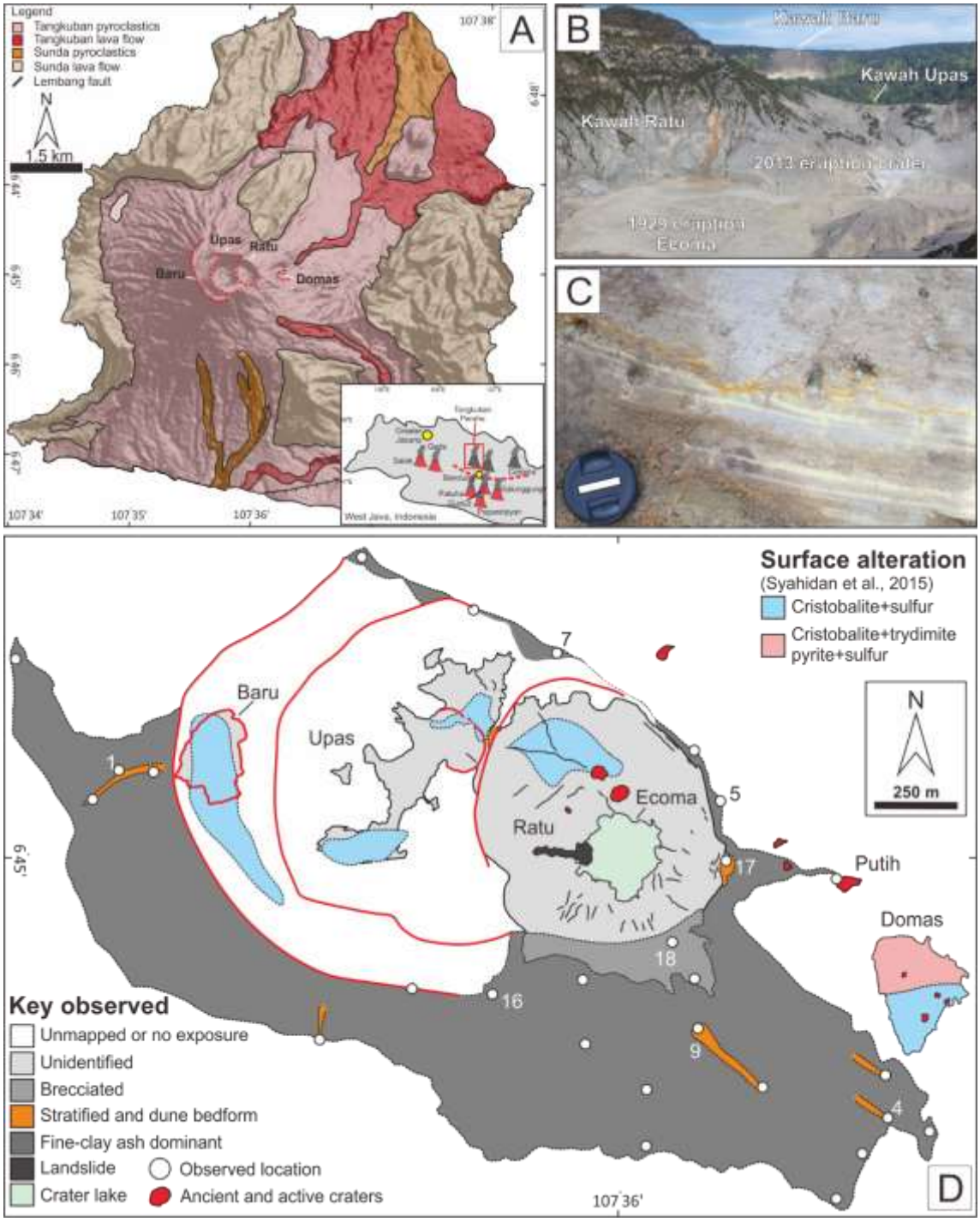

Figure 3.1. A) Map showing the location of Tangkuban Parahu volcano, as well as general geological information (modified after Nasution et al., 2004). B) The photograph displays the summit area and active craters (Baru, Ratu, Upas), which includes the Ecoma vent (the 1929 eruption) and the 2013 crater. C) The photograph shows an example of volcanic products from the proximal area of Tangkuban Parahu volcano. D) Compiled geology (see Chapter 2) and surface alteration map (Syahidan et al., 2015). Surface hydrothermal alteration consists of cristobalite and sulfur alteration at Ratu, Upas, and Baru craters, whereas Domas crater covered by two alteration types, consisting of cristobalite, tridymite, pyrite, and sulfur

Figure 3.2 Composite log of the proximal tephra succession, together with compiled mineral assemblages in the studied ash particles from x-ray diffraction and petrographic analyses. The volcanic products are composed of tephra deposits ranging from fine-clay ash to pyroclastic breccia. Note that all occurrences of mineral phases were plotted based on the ratio between the measured peak of minerals and quartz standard intensities. Hydrothermal minerals are associated with silica polymorph (quartz, cristobalite, and tridymite) and alunite, whereas kaolinite and jarosite crystals were found in the upper portion of studied tephra succession. In optical and electron microscope observations, a total of 351 ($\bar{x}_{\text{Observation}} = 23$ ash particles; $1 \leq \boldsymbol{\phi} \leq 2$ and $3 \leq \boldsymbol{\phi} \leq 4$) ash particles were observed. Hydrothermal minerals are predominantly comprised of silica, silica+alunite, silica+alunite±kaolinite, and alunite+jarosite, as well as fresh and altered magmatic juveniles in Unit 1, 2, 4, and 6.

3.3.2. Sulfur isotope

Sulfur isotope analysis was performed to constrain the sulfate and sulfide formations. A total of 21 samples was collected, consisting of alunite, jarosite, and pyrite. Alunite crystals were handpicked from the ash fraction of $1 \leq \phi \leq 2$ in size, which mostly sampled from yellow and pinkish ash particles. Jarosite was sampled from highly oxidized tephra layer in Unit 8 (see Fig. 3.2). Free crystal of pyrite is absent; therefore, the pyrite crystals were tried to extract from the handpicked silica-rich ash particles. All samples were ground to a fine powder, before further chemical separation and decomposition of sulfates and sulfides, respectively.

Sulfates (alunite and jarosite) were dissolved with 0.5 N NaOH at 80 ℃ (Watanabe and Hedenquist, 2001; Manalo et al., 2018), whereas sulfides (pyrite) were decomposed with 20 mL of HNO_3 and 2 mL of Br_2 solutions at 90 ℃, then converted to $BaSO_4$ by adding $BaCl_2 \cdot 2H_2O$. $BaSO_4$ was packed with V_2O_5 in tin foil (Yanagisawa and Sakai, 1983). The sulfur isotopic concentrations were measured by mass spectrometer using a Thermo Fisher Scientific Delta V at Faculty International Resource Science, Akita University. Seawater sulfate (IAEA-NBS-127) and barium sulfate (IAEA-SO-5 and IAEA-SO-6) were used as a standard, which was provided by the International Atomic Energy Agency (IAEA). Moreover, the isotopic ratios are presented with an expression of $\delta^{34}S$ per mil (‰) relative to the sulfur from Canyon Diablo Troilite (0.0450045 ‰) (Ault & Jensen, 1963).

3.4. Results

3.4.1. XRD result

In Fig 3.2, the ash mineralogy from XRD analysis is presented, whereas representative x-ray spectrums can be seen in Fig 3.3. Silica minerals are dominant. It consists of quartz, cristobalite, and tridymite, which shows the highest x-ray intensities almost in all samples. Alunite mostly displays weak-medium peak intensities, although it presents in all analyzed samples. 7Å kaolinite peaks show very-weak intensities in unoriented samples; thus, the spectrums were checked in oriented samples, only to validate their presence on the samples (Fig. 3.3). 7Å kaolinite occurs randomly in several tephra units of Unit 1 to 4 (Fig

3.2) without any indication of dickite x-ray pattern in those samples. Jarosite (Fe-rich hydrous sulfate) and goethite x-ray peaks appear in the samples mainly from the middle and upper portion of stratigraphic units (Unit 4, Unit 6, and Unit 8), although jarosite also appears in lower stratigraphic of Unit 2. Anatase (TiO_2 polymorph) appears in some samples from low to upper stratigraphic units (Unit 1, Unit 4, and Unit 7). It is noteworthy that 10-14 Å (i.e., smectite; muscovite) mineral group is absent in all analyzed samples.

Magmatic minerals also occur in the samples, consisting of plagioclase, sanidine, augite (clinopyroxene), orthopyroxene, and rutile. However, their presence of magmatic minerals is scattered in all tephra layers. A most important observation is that the orthopyroxene frequently occurs in some samples of the upper portion of tephra succession, where they are absent in most of the lower units. Moreover, the presence of anatase in some units may also indicate rutile (TiO_2) occurrence in the samples; although in-situ observation needs to be performed under Raman Spectroscopy.

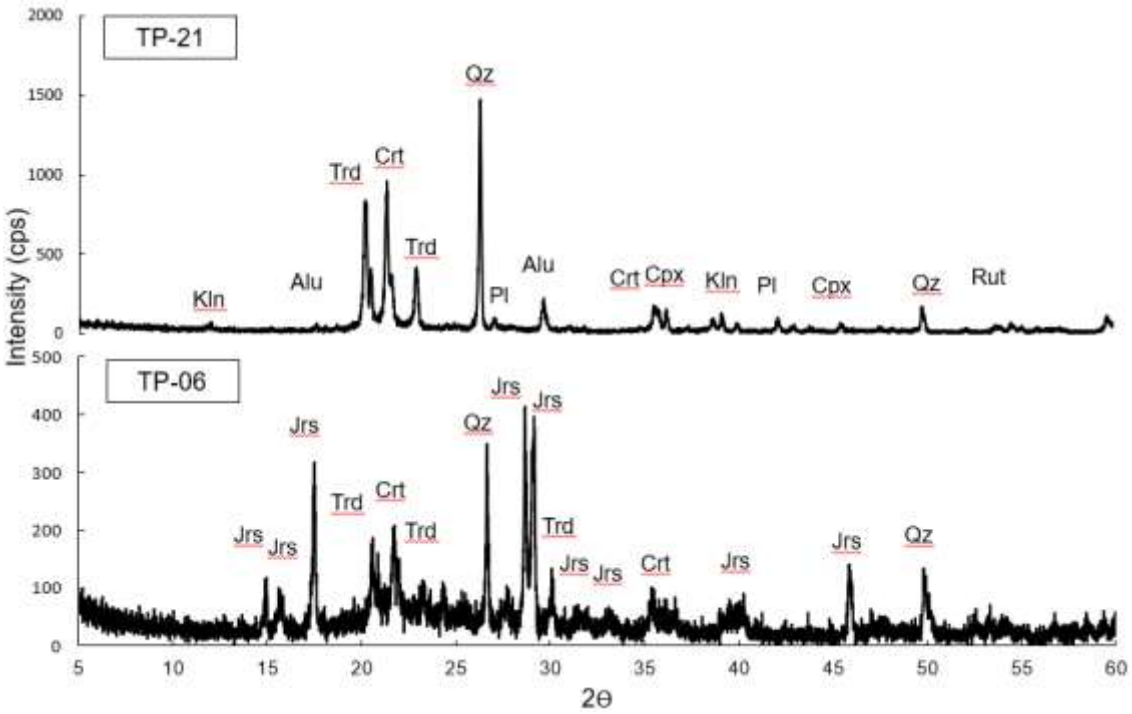

Figure 3.3. X-ray diffractograms of ash samples TP-06 (Unit 8) and TP-21 (Unit 3). Abbreviation; *Alu*: alunite, *Crt*: cristobalite, *Kln*: kaolinite, *Pl*: plagioclase, *Rut*: rutile, *Trd*: tridymite, *Jrs*: jarosite, *Qz*: quartz, *Cpx*: clinopyroxene.

3.4.2. Ash petrography

Distribution of petrographic observation is shown in Fig. 3.2. However, the distribution graph cannot be used as a representative proportion of each type of ash particles (i.e., silica, silica-alunite, silica-alunite±kaolinite, alunite-jarosite, and altered magmatic juvenile or glass), because it is difficult to generalize total proportion in the tephra layer from the current proportion of observed ash particles (n= 351, $\bar{x}_{\text{observation}}$ = 23 ash particles). (Fig 3.5.).

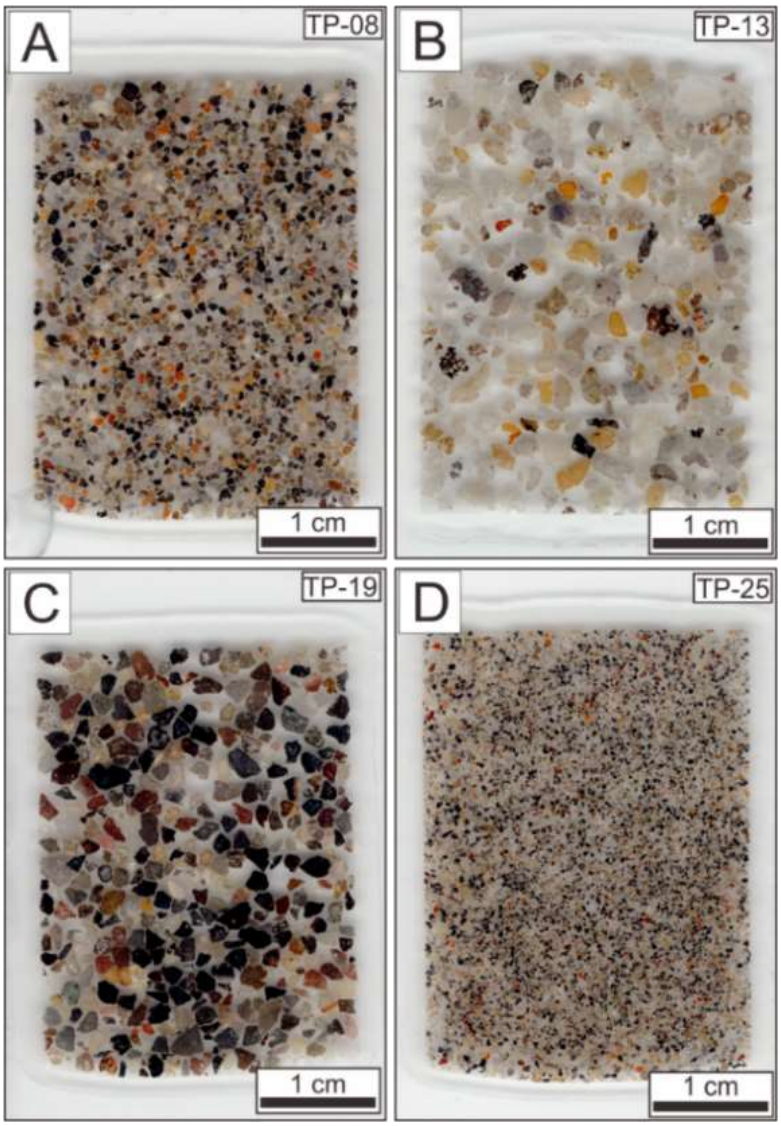

Figure 3.4. Scanned thin section from the tephra deposits showing four main types of volcanic products. A) Fine-clay ash with jarosite minerals, B) Fine-clay ash with silica-rich ash, C) Fine-clay ash with volcanic rock and hydrothermally altered fragments, D) Coarse ash with magmatic juvenile and hydrothermally altered fragments.

Most important information was displayed in the form of mineralogical documentation by XRD analysis (Fig 3.2). From XRD analysis, we noticed that the alteration assemblages mainly consist of silica polymorph and alunite, whereas kaolinite and jarosite appear in some volcanic products. Furthermore, both observations (i.e., XRD and petrography) suggesting similar mineral assemblages; therefore, this section will present the petrographic observation, in the context of detailed in-situ mineralogical assemblages and the textural relationship of hydrothermally altered fragments from observation under optical and electron microscopes. Here, the result of petrographic observation was divided into two sections, 1) altered magmatic juvenile or glass, and 2) hydrothermal mineral assemblages from selective to pervasive alteration ash particles.

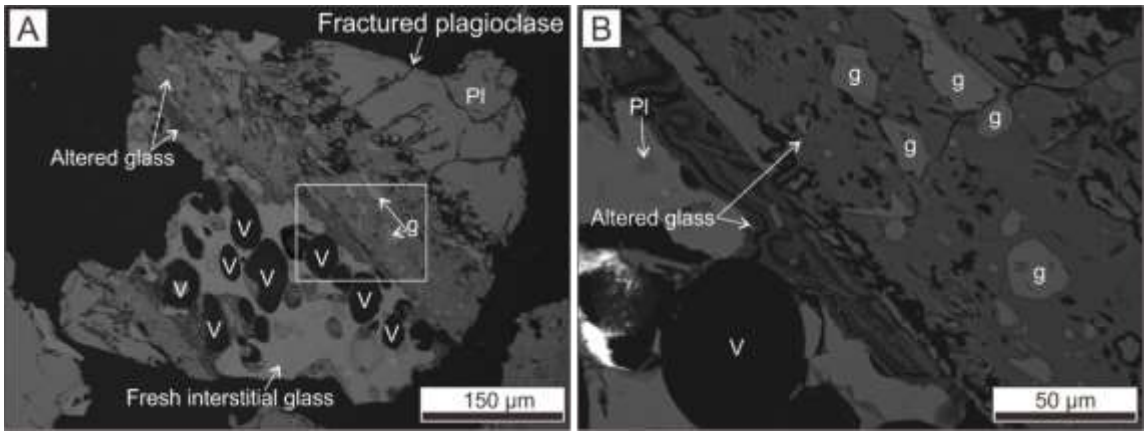

Figure 3.5. Backscattered electron images showing the examples of a partly altered magmatic juvenile in Unit 4 and 3. A and B) Altered interstitial glass in vesicular magmatic juvenile shows the colloform banding texture, which appears to be similar with epithermal quartz veins. Vesicles are clean from infilling hydrothermal minerals.

Altered magmatic juvenile or glass

Partly altered ash magmatic juvenile or glass was found in Unit 4 (TP14, TP18, TP19). The magmatic juvenile contains fresh interstitial glass as well as altered lithics, where the vesicular textures are commonly found within the fresh interstitial glass. Altered glass zonation is narrow in thickness (~10 mm) and associated with hydrothermally altered lithics (>50 µm in thickness). Hydrothermal minerals are commonly absent or unidentified. For instance, there are no infilling hydrothermal minerals in vesicles, which commonly found in some altered magmatic juvenile in other types of ash particles (selective or pervasive altered ash particles).

Hydrothermal minerals in selective to pervasive alteration ash particles

Petrographic and Raman spectroscopy revealed two general types of hydrothermal alteration in the proximal volcanic products of Tangkuban Parahu volcano, by the following;

1. Alunite alteration represents the most abundant alteration types (~60 %, from the total petrographic observation) from the volcanic products (see Fig 3.2). It is associated with several hydrothermal minerals, comprising opal, cristobalite, quartz, and kaolinite. This alteration including the presence of alunite-jarosite in some ash particles.

2. Quartz (residual silica) alteration represents the second most abundant alteration types (~30 % from the total petrographic observation) in the volcanic products (see Fig 3.2). Alteration is strong to moderate in intensity. It is only associated with accessory minerals. Accessory minerals are anatase, pyrite, magnetite, titanomagnetite, and ore minerals.

These two hydrothermal mineral associations are further breakdown to five specific alteration types, along with two veinlet feeders in the ash particles. The alteration types were defined based on the dominant hydrothermal minerals within a single ash particle.

Opal alteration

Opal was found mostly in vesiculated ash particles (Fig 3.7A-D). It shows a prominent Raman spectrum at 267, 508, 561, and 782 cm^{-1} (Fig 3.6). Hydrothermal minerals also found in vesicular textures, which are composed of silica minerals. In the examined ash particle, opal selectively altered the magmatic minerals (clinopyroxene; $En_{35}Wo_{34}Fs_{29}$ and plagioclase; $An_{47}Or_{04}Ab_{49}$) and produced pseudomorph textures (prismatic and hexagonal shape; >50 µm in size). Alteration intensity is weak to moderate; thus, the remnant of plagioclase and clinopyroxene can be observed (Fig 3.5B-D), as well as unaltered microlites of augite and pigeonite. For the interstitial glass, the focus was not given to the characterized the alteration intensity in interstitial glass; but, judging from the degree alteration in the igneous crystals. It assumed that the interstitial glass has had also experienced an alteration by the hydrothermal fluid.

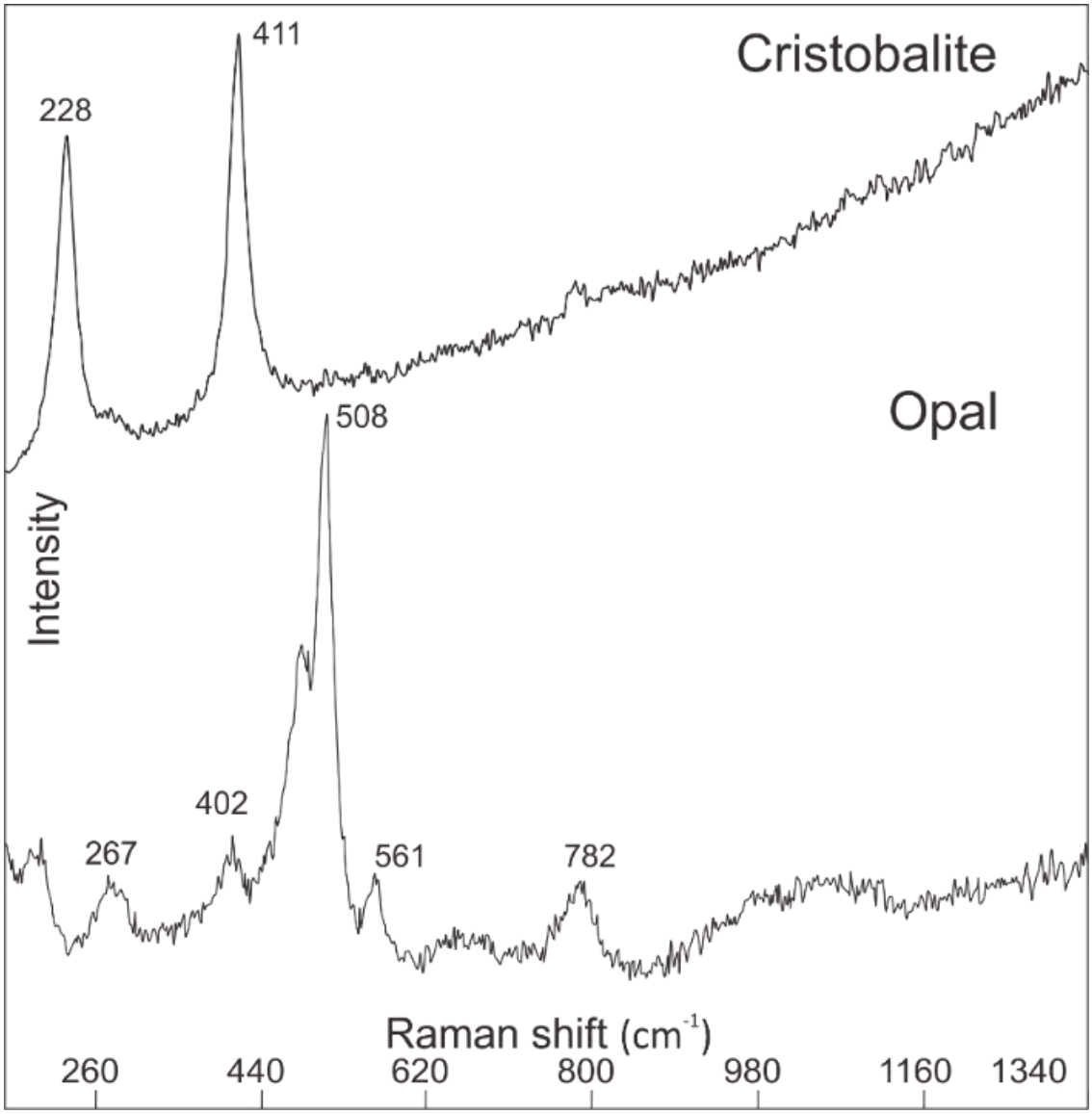

Figure 3.6. Graph showing the two representatives Raman spectrum of cristobalite and opal in ash particles, specifically in Fig 3.7.

Opal-cristobalite+alunite±kaolinite alteration

The opal-cristobalite-alunite±kaolinite alteration was only found in dense ash particle (Fig. 3.7E-F), where the vesicular texture is absent. Opal is commonly associated with cristobalite. Cristobalite occurs as a cluster of conchoidal (<1 μm in diameter) shape substances, which was examined at the core of pseudomorphic texture (Fig. 3.7E), whereas opal minerals were found at the rim. Pristine cristobalite crystals display a Raman spectrum at 226 and 411 cm^{-1} (Fig. 3.7). Groundmass alteration (Fig 3.6E) consist of

alunite, silica, kaolinite, and anatase. Those crystals mostly occur as an anhedral with a size of 5-10 μm.

In figure 3.6E, a similar mineral assemblage was observed in other altered juvenile particles, although it displays a different pattern of alteration. Interstitial glass is altered pervasively, and fresh component (i.e., magmatic minerals) is absent. Opal, cristobalite, and alunite were entirely replaced the igneous minerals. Opal and cristobalite appear to be similar to the previous examples (Fig. 3.6D) although there is no relict of igneous minerals and cristobalite cluster in the pseudomorphic crystals. Alunite occurs as a large (>50 μm) crystal and irregular zoning, which replaced likely plagioclase crystals. Moreover, the alunite crystal was found locally associated with kaolinite at the pseudomorphic rim (Fig 3.6E).

Quartz-alunite±kaolinite alteration

Quartz-alunite±kaolinite alteration (Fig. 3.8A-D) was predominantly found in a subrounded to rounded ash particles. This association is the most abundant alteration assemblages. Quartz occurs alongside the alunite crystals, as subhedral to euhedral fine-grain (<10 μm) crystals. Alunite occurs as euhedral, elongated lath (<10 μm in length) (Fig. 3.8B), and zoned crystals (>5 μm in diameter) (Fig. 3.8D). They mostly have an intermediate composition of Na and K with a concentration K_2O of 3.39-5.74 wt.% and Na_2O of 0.21-1.18 wt.%. In some ash particles, huangite (Ca-alunite; Li et al., 1992) was rarely found, although it is not wholly absent. Huangite crystals commonly occur as an accessory mineral in pervasive quartz ash particles, along with anhedral anatase, kaolinite, pyrite, and chalcopyrite assemblages. In some ash particles, kaolinite commonly occurs as a circular shape cluster fine-grained crystals (Fig 3.8A-D).

Alunite-jarosite alteration

Alunite and jarosite are found in highly porous ash particles (Fig 3.8E-F). Void or pore zones mostly occupied by the mixture of silica mineral. Alunite crystals occur as subhedral to euhedral with >10 μm in size. Jarosite is most common in the alunite-jarosite intergrown. Ti-oxide occurs as an accessory mineral, which most likely anatase.

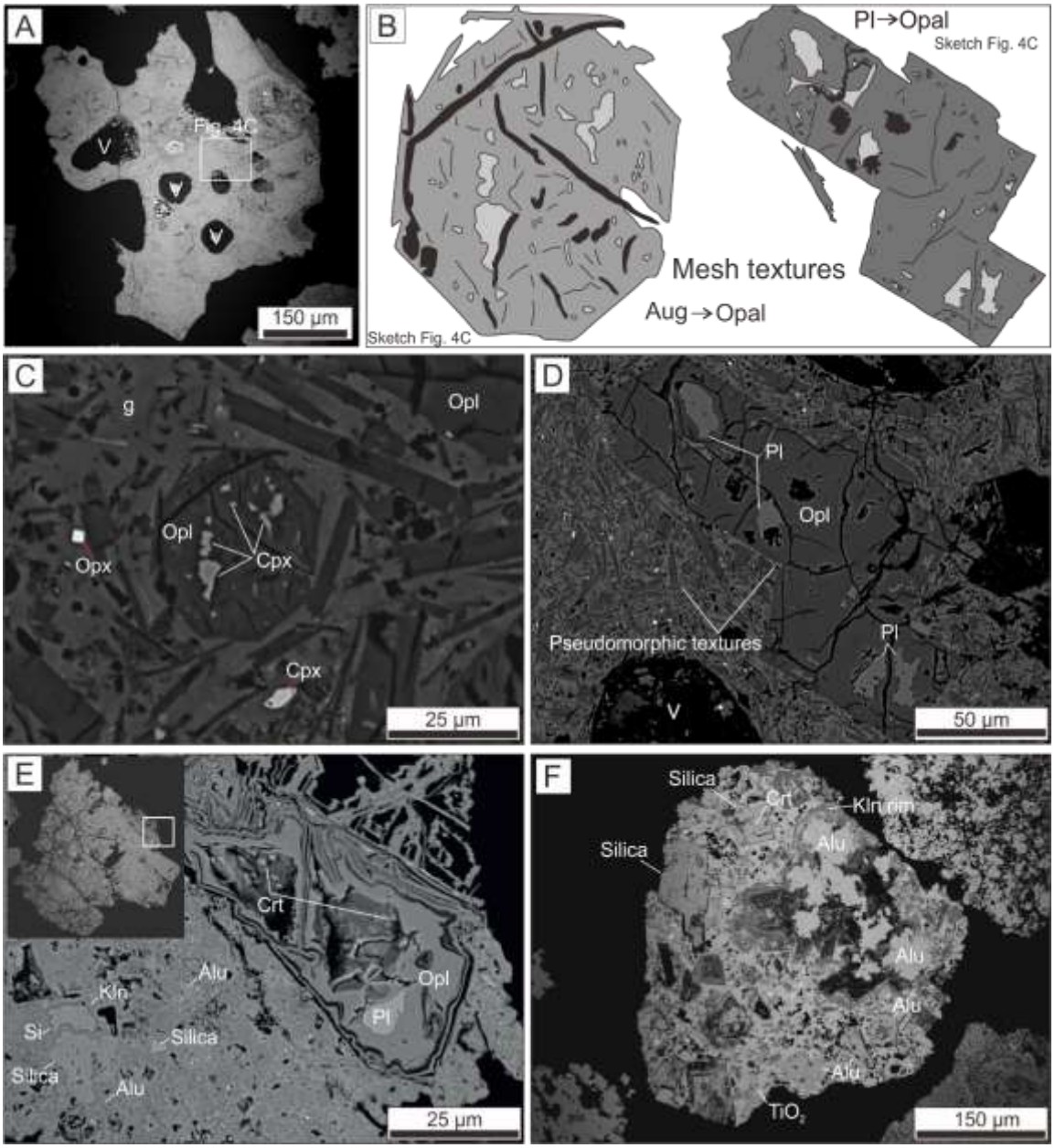

Figure 3.7. Backscattered electron images showing the textural features of opal and opal-cristobalite±alunite±kaolinite in ash particles. A) Opal alteration was found on vesiculated protolith. Vesicular textures were filled with silica minerals. B) Mesh texture of clinopyroxene and plagioclase (Fig. 3.7 C and D). Opal was replaced both magmatic minerals. E) BSE image shows opal-cristobalite after plagioclase, whereas silica-alunite±kaolinite occur as a groundmass alteration. F) Opal-cristobalite-silica-alunite sporadically replaced the magmatic minerals in dense ash particle. Most of the hydrothermal minerals occur as pseudomorphic texture.

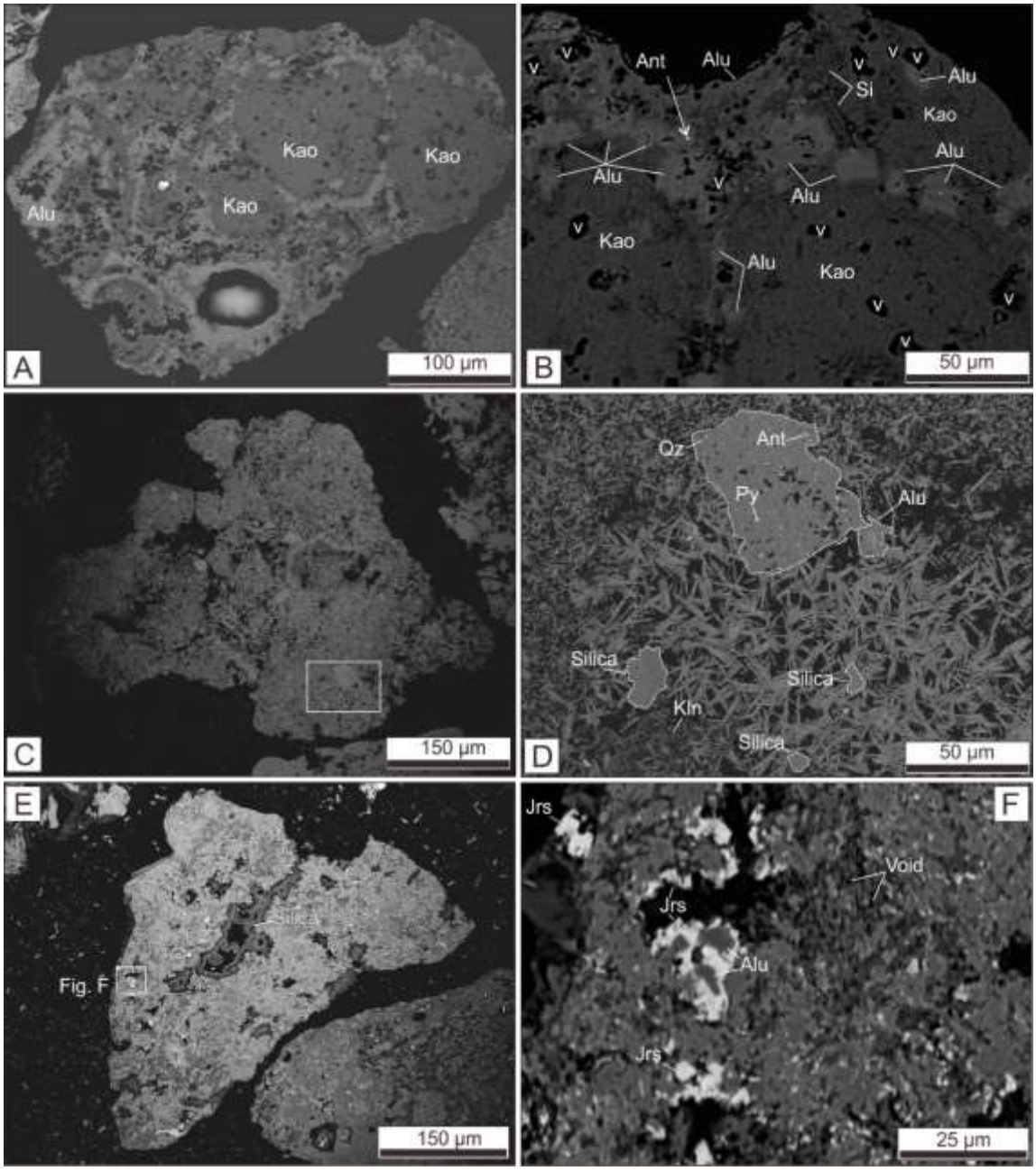

Figure 3.8. Backscattered electron images showing the textural features of quartz-alunite±kaolinite and alunite-jarosite alteration assemblages in ash particles. A and B) Alunite occurs as equant crystal shape, which is associated with circular kaolinite crystal cluster, anatase, and quartz. C and D) Quartz-alunite±kaolinite alteration. Alunite occurs as elongated-tabular lath and interstitial quartz±pyrite±anatase alteration. E and F) Alunite-jarosite was found in subangular to subrounded ash particle. Jarosite occurs as alunite-jarosite intergrown texture. Both minerals are associated with silica mineral that mainly occurs as pore-filling minerals. Silica (unidentified polymorph phase).

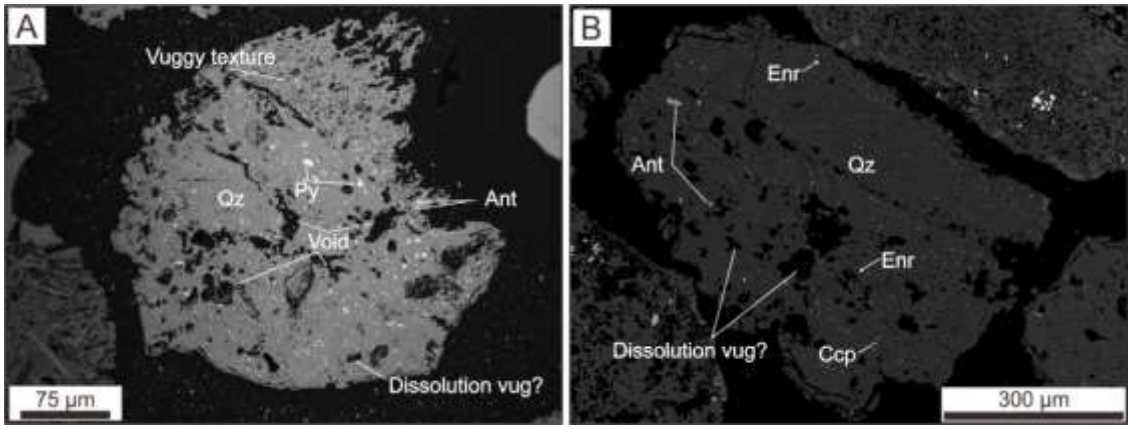

Figure 3.9. A) BSE image displays subangular to subrounded ash fraction, which had been pervasively altered by quartz. Noted, on the edge of ash fraction, a vuggy texture develops and fill up by anhedral and elongated shape pyrite. B) Another example of ash fraction with pervasive quartz alteration. The quartz is subordinate with anatase, enargite, chalcopyrite, titanomagnetite, and magnetite. Abbreviation: Enr: enargite, Ccp: chalcopyrite.

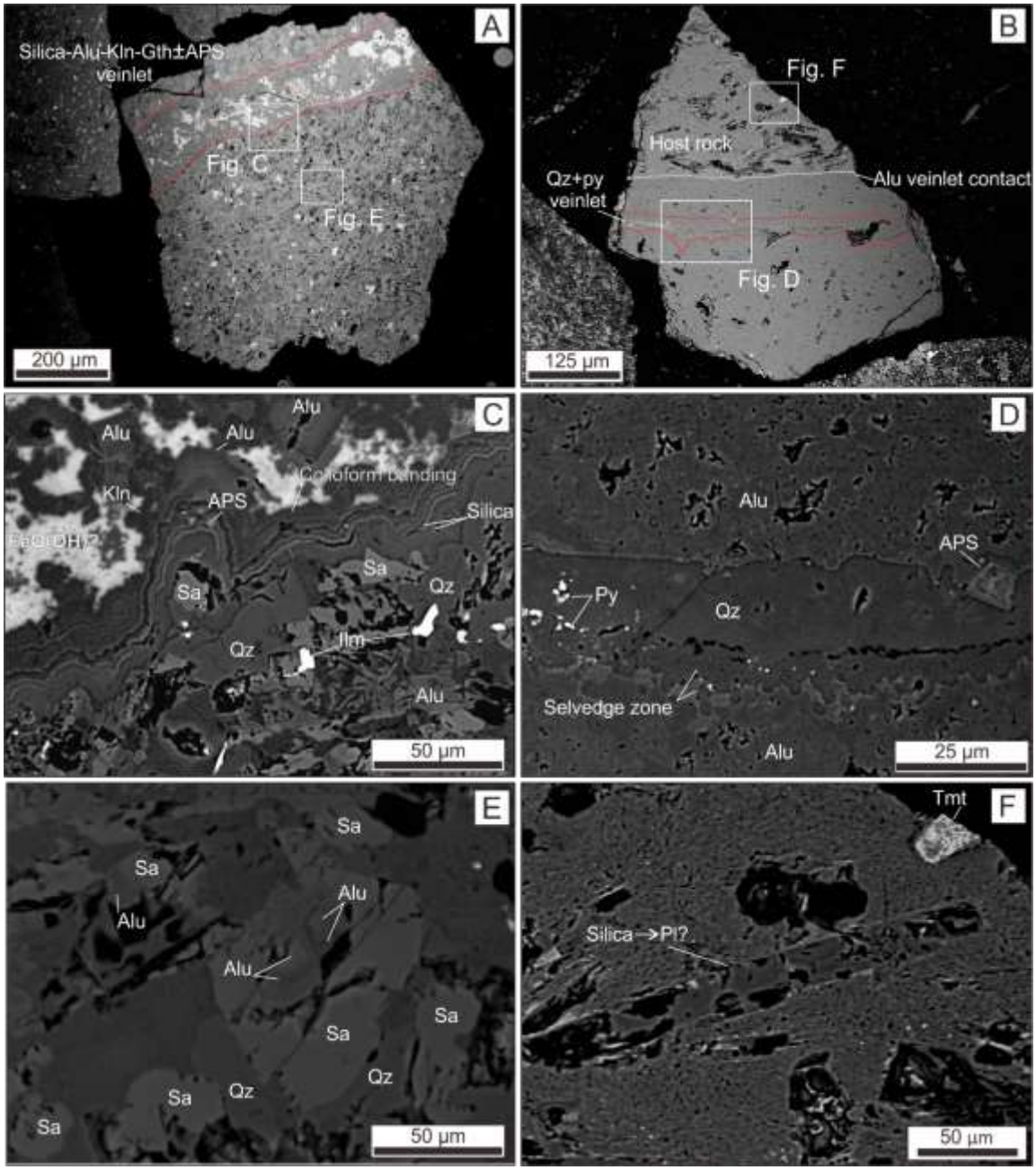

Figure 3.10. Backscattered electron image showing two examples of the feeder veinlet in different host rock. A, C, and E) BSE images show the host-rock (holocrystalline-porphyritic) and silica-alunite-kaolinite-FEOOH (goethite?) veinlet. The host rock is composed of quartz, sanidine, titanomagnetite, and rutile. Fig. E display intense alteration of host rock by silica mineral and sanidine replacement by alunite. B, D, and F) BSE images shows the host rock (porphyritic rock), alunite zone, and quartz-pyrite veinlet.

Quartz alteration

Quartz alteration (Fig. 3.9A-B) was found in an angular to subangular ash particles. Vugs occurs as rectangular and elongated, indicating dissolution of original crystals by alteration (Fig 3.9A). Quartz crystals have had pervasively altered the protolith and occur as a euhedral, equant, and pure SiO_2 (98-100 wt.%) concentration; such crystals commonly formed an interlocked mosaic cluster. Crystals vary in size, range from 10 to 50 µm. Quartz mostly has a high modal proportion of 90-95 vol %. Accessory minerals are anhedral and elongated titanomagnetite, magnetite, pyrite, chalcopyrite, and enargite with <5 µm in diameter (Fig. 3.9B). These minerals occur as pore-filling minerals and disseminate throughout the ash surface with a total concentration of <1 vol%.

Silica-alunite-kaolinite-goethite veinlet feeder

Silica-alunite-kaolinite-goethite veinlet was found in a holocrystalline-porphyritic host rock (Fig 3.12, A, C, and E). Minerals in host rock consist of quartz, sanidine, ilmenite, titanomagnetite, and rutile. Most of the minerals have had experience intense silicification (SiO_2 contents 65- 79 wt.%). Alunitization also sporadically altered the euhedral sanidine ($An_{04}Or_{56\text{-}74}Ab_{22\text{-}40}$) crystals in host-rock (Fig 3.12.E).

The veinlet is ~50 µm in thickness. Mineral assemblages consist of unidentified silica phases (SiO_2 contents of 55-72 wt.%), anatase, aluminum-phosphate-sulfate (APS), kaolinite, goethite, and alunite (Fig 3.12 C). Several unidentified silica phase veinlets are enclosed to the host-rock and occur as colloform textures (Dong, 1995), which indicates open-fracture filling during early-stage veinlet deposition. APS occurs as very-fine crystal inclusions in alunite veinlet (<5 µm in thickness). Alunite occurs as euhedral, zoned crystals (10-20 µm in diameter), and mostly replaced by kaolinite-goethite intergrown. Moreover, alunite crystals in the vein are mostly rich in K concentration, which is suggested from EDS data (see appendices for chapter 3).

Quartz-pyrite veinlet feeder

Quartz-pyrite veinlet was found to develop on pervasive alunite zone in a porphyritic host rock (Fig. 3.8 B, D, and F). Host rock had been extremely silicified. It consists of silica after likely plagioclase and subhedral titanomagnetite (Fig 3.7 B and F), whereas the

alunite zone comprises ~50 vol.% of the ash particles. Alunite zone mainly contains Na-K alunite, together with aluminum-phosphate-sulfate (APS) in contact with the quartz-pyrite veinlet. Quartz-pyrite veinlet is 15-20 μm in thickness. Quartz in veinlet displays a uniform BSE image band (Fig. 3.7 C). Pyrite crystals occur as an anhedral (<5 μm in diameter), subrounded to rounded, and centreline bleps pyrite in quartz crystals. The selvedge zone provides information on the relative timing of quartz-pyrite veinlet after alunite zone (Fig. 3.7 C), whereas the mineralogy of selvedge zone mainly consists of silica minerals in association with very-fine alunite crystals.

3.4.3. Sulfur isotope

The $\delta^{34}S$ value of alunite varies from 2.81 to 20.81‰ (n:19; avg. 9.02). They are lighter in the upper stratigraphy (Unit 6, 7, and 10) than those in the lower stratigraphy (Unit 4, 3, 2, and 1), although some of the alunite display low $\delta^{34}S$ values in Unit 4. Furthermore, the $\delta^{34}S$ values of pyrite are naturally lighter (-2.75‰ and -3.5‰) than alunite. Jarosite yielded a $\delta^{34}S$ value of -1.58‰, which is close to the sulfide values.

Table 1. Summary of ‰^{34}S values from sulfides and sulfates in selected volcanic products.

No	Sample ID	Lithologies	Minerals	‰ ^{34}S
1	TP01	Pyroclastic breccia	Alunite	5.02
2	TP07	Pyroclastic breccia	Alunite	5.64
3	TP09	Fine-clay ash	Alunite	2.81
4	TP09	Fine-clay ash	Alunite	5.77
5	TP11	Lapilli tuff	Alunite	5.09
6	TP12	Fine-clay ash	Alunite	7
7	TP13	Lapilli tuff	Alunite	10.6
8	TP13	Lapilli tuff	Alunite	10.67
9	TP14	Fine-clay ash	Alunite	9.6
10	TP15	Coarse ash	Alunite	20.81
11	TP16	Fine-clay ash	Alunite	5.68
12	TP17	Coarse ash	Alunite	10.2
13	TP20	Coarse ash	Alunite	13.52
14	TP21	Fine-clay ash	Alunite	9.40
15	TP22	Fine-clay ash	Alunite	11.74
16	TP23	Fine-clay ash	Alunite	9.23
17	TP24	Fine-clay ash	Alunite	8.49
18	TP25	Coarse ash	Alunite	11.1
19	TP02	Fine-clay ash	Jarosite	-1.58
20	TP 15	Coarse ash	Pyrite	-2.75
21	TP15	Coarse ash	Pyrite	-3.5

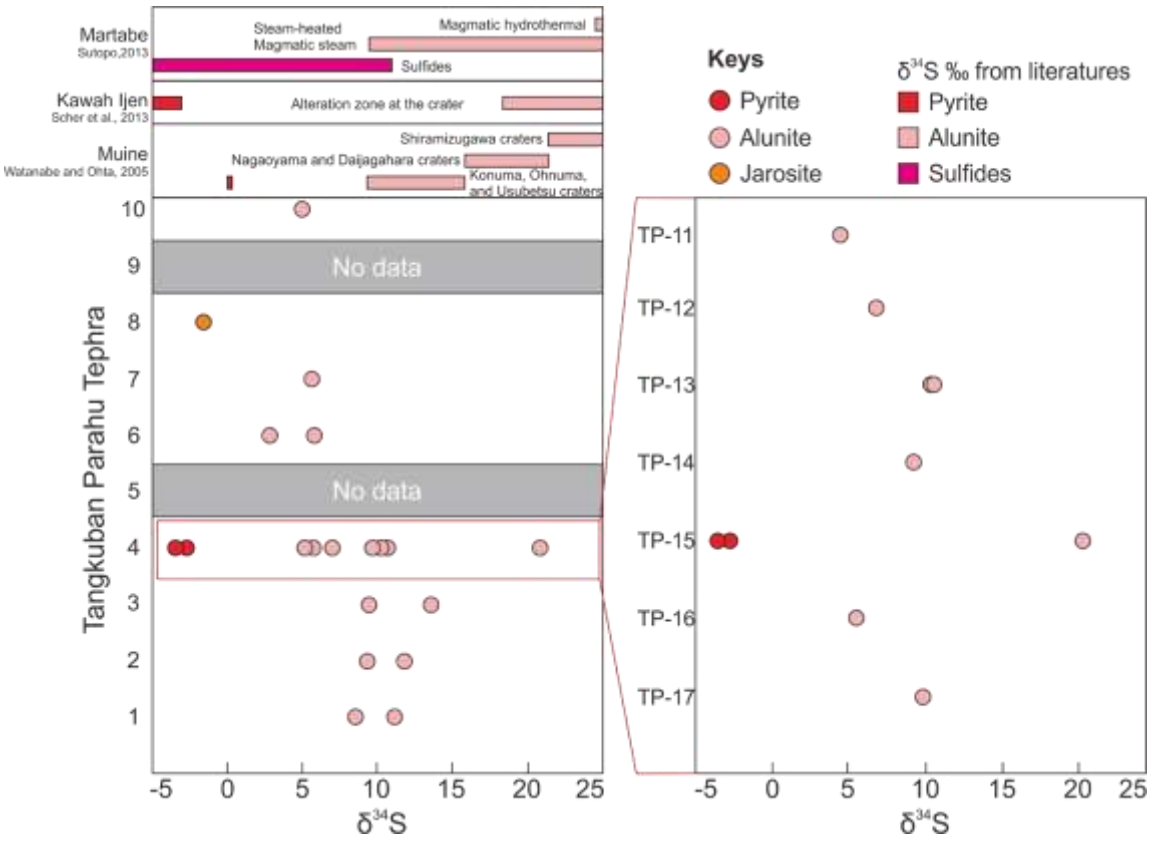

Figure 3.10. Graph showing the plot of the $\delta^{34}S$ value of alunite, pyrite, and jarosite against the stratigraphic unit (older to younger). The $\delta^{34}S$ values are compared with $\delta^{34}S$ values from Mt. Muine (Watanabe and Ohta, 2005), Kawah Ijen (Scher et al., 2013), and Martabe (Sutopo, 2013).

3.5. Discussion

In this chapter, the present work on ash characterization, including mineralogical, petrographic, and sulfur isotopic studies of the volcanic products provides critical information for the volcanic-hydrothermal system at the upper-level of Tangkuban Parahu volcano edifice. The discussion will elaborate on the hydrothermal environment, sulfide and sulfosalt formation, and sulfur isotopic variation from studied ash particles, and the implication of this study on the phreatic eruption.

3.5.1. Hydrothermal and oxidation environment

The hydrothermal minerals of studied ash particles from XRD and petrographic observations comprise opal, opal-cristobalite-alunite±kaolinite, quartz+alunite ± kaolinite, and quartz alteration. The mineral assemblages suggest that silica minerals are dominant in volcanic products. Their presence appears to be similar to the mineralogy in

some localities within the active craters, where cristobalite and tridymite were identified at Ratu, Domas, and Upas craters (Syahidan et al., 2005), although opal and quartz have never been found and observed within the active craters. Opal and cristobalite are commonly precipitate under low pressure and temperature (Fournier, 1985), which probably formed within a range of temperature from 100 to 150 ℃. Both silica phases mostly formed by extreme silicification in protolith, which is associated with the cation leaching process (; plagioclase; Ca^{2+}, K^{2+}, Na^{2+}, Al^{2+}; Augite; Ca^{2+}, Mg^{2+}, Fe^{2+}; Fig 3.12.) and possibly dissolution of magmatic juvenile by extreme acidic fluid (Hedenquist et al., 1994; Van Hinsberg, 2010; Hedenquist and Taran, 2013).

Quartz is the most abundant silica mineral, which only crystallized at relatively high temperatures. Thus, the formation temperature of cristobalite cannot be applied to constraint the quartz crystallization. The presence of quartz and kaolinite in petrographic observation can be used to estimate formation temperature by applying mineralogical reaction in the Al_2O_3-SiO_2-H_2O system (Chaterjee et al., 1984; Hemley et al., 1980). The reaction can be written as follow for the Al_2O_3-SiO_2-H_2O system;

$$\text{kaolinite} + 2\ \text{quartz} = \text{pyrophyllite} + H_2O \qquad (1)$$

$$\text{pyrophyllite} = \text{andalusite} + 3\ \text{quartz} + H_2O \qquad (2)$$

$$\text{pyrophyllite} + 3\ \text{diaspore} = 4\ \text{andalusite} + 4\ H_2O \qquad (3)$$

All equations have equilibrium temperatures at 260-280 ℃ (1), 300-340 ℃ (2), and <320 ℃ (3). Andalusite, diaspore, and pyrophyllite (in equation 2 and 3) are absent in observed mineral assemblages, indicating the temperature of quartz and kaolinite formation are possibly less than 340 ℃. Therefore, the equilibrium temperature of <260 ℃ is reliable to explain the hydrothermal condition of quartz and kaolinite formation in the volcanic field.

Tridymite was found in volcanic products during the course x-ray diffraction, although it cannot be located and observed by coupled in-situ observation using petrography and Raman Spectroscopy. Therefore, the occurrence of tridymite remains unknown. In ash particles, many previous works (e.g., Ohba and Kitade, 2005) suggest that tridymite crystals commonly formed under magmatic conditions, which most likely present in some coherent and magmatic juvenile components in the volcanic products.

Alunite is the most abundant sulfur-bearing mineral in Tangkuban Parahu volcanic products. Alunite crystals are interpreted to be formed by the condensation of magmatic-steam (Rye et al., 1992; Rye et al., 1993) as indicated from petrographic observation, which also marked the acidic fluid (Reed, 1997; Ohba and Kitade, 2005) role during the alteration process. Alunite mostly occurs as elongated lath, zoned and replacement crystals. Those textures probably indicate that alunite was crystallized during a complex series of overprinting hydrothermal alteration, where zoned texture in alunite represents several injections of magmatic steam (Aoki, 1991).

Table 2. Summary of assigned temperature from the mineral assemblages.

Assemblages	Temperature (°C)	Literatures
Opal-cristobalite	100-150 °C	Fournier, 1985
Quartz±kaolinite	<260 °C	Hemley et al., 1980; Chaterjee et al., 1984
Alunite	<250 °C	Watanabe and Hedenquist, 2001
Alunite±aluminum-phosphate-sulfate	>250 °C	Stoffregen and Alpers, 1987
Alunite-jarosite	100-300 °C	Stoffregen et al., 2000

In some ash particles, alunite commonly associated with APS, indicating the formation temperature of 250 ℃ (e.g., Watanabe and Hedenquist, 2001). Moreover, the phosphate concentration in hydrothermal minerals (i.e., APS) is possibly related to dissolves magmatic apatite that releases phosphate at magmatic temperature (Stoffregen and Alpers, 1987); thus, phosphate-bearing alunite together with the aluminum-sulfate-phosphate is the hypogene origin. Moreover, alunite crystals that appear without any occurrence of APS minerals are mostly crystallized at a temperature <250 ℃, as it is documented in many hydrothermal ore deposits (e.g., Arribas, 1995; Watanabe and Hedenquist, 2001). Furthermore, the geothermometer of sulfate and sulfide was applied by using the fractionation equation from Ohmoto and Rye (1979) and Ohmoto and Lasaga (1982), assuming the alunite and pyrite naturally equilibrium. The equilibrium temperature is 232 ℃ and 240 ℃, which shows an almost similar range of formation temperature with assigned temperature from mineral assemblages.

To better understand the origin of alunite in the samples, the $\delta^{34}S$ results was compared with several available datasets of $\delta^{34}S$ values from Mt. Muine (Watanabe and Ohta, 2005), Martabe deposit (Sutopo, 2013), and Mt. Ijen (Scher et al., 2013) (Fig. 3.12) The $\delta^{34}S$ values of Tangkuban Parahu volcanic products range from 2 to 20.81‰. These values are consistent with Wanatabe and Ohta (2005). Watanabe and Ohta (2005) were interpreted that the $\delta^{34}S$ values below 20 ‰ were classified as magmatic-steam alunite, whereas the $\delta^{34}S$ values higher than 20 ‰ is falling into a magmatic-hydrothermal alunite field. This suggestion is consistent with a broader range of $\delta^{34}S$ values of alunite in Martabe high sulfidation deposit (Sutopo et al., 2013). Moreover, if we take the $\delta^{34}S$ values of alunite (18-20 ‰) in Mt. Ijen into our consideration, then the alunite with $\delta^{34}S$ values 20.81‰ is magmatic-hydrothermal alunite. However, there is no evidence of magmatic-hydrothermal alunite, which commonly judges by the presence of a significant amount of alunite-pyrite association (Rye et al., 1993) in one section of ash particles. Therefore, the $\delta^{34}S$ values of alunite, coupled petrographic observation, and sulfur isotopic values clearly suggest that the alunite crystals in the volcanic products are the magmatic-steam origin.

Sulfide (pyrite and chalcopyrite) and sulfosalt (enargite) minerals occur in volcanic products at Tangkuban Parahu volcano, although their occurrence rarely found in many ash particles. The ore minerals occur as anhedral crystals in vuggy texture, suggesting that it was precipitated from a vapor condensate (William-Jones et al., 2002), as filling pore of intensely altered leached volcanic rock (Arribas, 1998; Hedenquist et al., 2000). This texture is quite like those the enargite deposit in the high sulfidation ore deposit (Hedenquist and White, 1992; Arribas, 1995). Moreover, their presence has been documented in volcanic products from phreatic eruption (e.g., Papandayan; Mazot, 2008).

Jarosite crystals are observed in some volcanic products and associated with alunite. Jarosite can form at a temperature range from ~100 to ~300 ℃ (Stoffregen et al., 2000) by pervasive oxidation of sulfide minerals. However, the sulfide minerals are incredibly uncommon in oxidized ash particles and no evidence of partly oxidized sulfides in the samples. Therefore, the $\delta^{34}S$ value of the jarosite-rich layer in Unit 8 can be used to explain the origin of jarosite. Rye et al. (1992) observed the similarity of $\delta^{34}S$ values from secondary sulfate minerals to sulfide phases. The $\delta^{34}S$ values of jarosite and pyrite are almost identical -1.58 ‰, and -2.75‰ and -3.5‰, which is consistent with Rye et al.

(1992). This observation can be used to explain the jarosite after pyrite in the volcanic products.

Furthermore, it is essential to note that jarosite occurs with goethite in some volcanic products. Jarosite and goethite indicate the involvement of atmospheric oxygen (i.e., surface condition) during the oxidation process. The alunite in alunite-jarosite intergrowth most likely formed under the assigned temperature (<250-250 ℃), where such temperature gradient can be established only underneath the crater; thus, the jarosite potentially formed after the process of fragmentation of volcanic products.

3.5.2. Synthesis on hydrothermal and geological environment

As described, the hydrothermal minerals in the volcanic products of Tangkuban Parahu represent a complex episode of acid-sulfate (Rye et al., 1992; Rye et al., 1993) or advanced argillic alteration (Arribas, 1995; Hedenquist and Taran, 2013), which mostly crop out at the active crater summit of stratovolcanoes (see. Mt. Ijen; Scher et al., 2013).

As mentioned above, cristobalite and opal can only be formed at a relatively low temperature (Fournier, 1985); such temperature range is mostly recorded at the near-surface summit craters. The presence of opal-A had been documented in Indonesian volcanoes by Lowernstern et al., (2018). They showed the opal-a selectively altered the pumice rocks and suggested that the opal-a crystallized before the eruption from the near-surface alteration below the crater lake of Mt. Ijen. This interpretation can be used to constrain the geological condition for similar volcanic products at Tangkuban Parahu, which also probably formed below the crater-lake of Ratu Crater.

Advanced argillic alteration (quartz, alunite, and kaolinite) present below the crater with the range of temperature of 250-300 ℃, which indicates that volcanic products were ejected from at least 300 m from the surface of craters. At this point, the result of mineralogy suggests that most of the ash particles were derived from the crater-conduit at a temperature below 300 ℃. Moreover, the advanced argillic alteration also possibly rooted in the higher temperature vapor zone (c. 300-400 ℃) (e.g., Hedenquist et al., 1996; Watanabe and Hedenquist, 2001) on top of crystallized porphyritic intrusion at depth (e.g.,

Sillitoe, 2010). This interpretation in agreement with a geothermal field model in calc-alkaline stratovolcanoes (see Hedenquist et al., 1996; Nemcok et al., 2007).

3.6. Conclusion

In this chapter, mineralogy, petrography, and sulfur isotopic were observed and documented from the hydrothermally altered lithics of Tangkuan Parahu volcanic products. The following is the conclusion of all observations;

Hydrothermally altered lithics consist of altered magmatic juvenile or glass, as well as selectively to pervasively altered ash particles. In altered magmatic juvenile or glass, the hydrothermal fluid mainly altered the interstitial glass of magmatic component. Hydrothermal alteration consists of opal, opal-cristobalite-alunite±kaolinite, quartz+alunite±kaolinite, and quartz alteration. Those alteration types mostly associated with accessory minerals of anatase, sulfide (pyrite and chalcopyrite), sulfosalt (enargite), magnetite, titanomagnetite, and APS minerals. Moreover, in some ash particles, the alunite alteration is also associated with jarosite. The first documentation silica-alunite-kaolinite-goethite±APS and quartz-pyrite veinlets were observed from the explosive volcanic products. It represents the magmatic vapor and hydrothermal fluid pathways below the summit craters.

The hydrothermal minerals reflect the temperature formation range from ~100 to ~300 ℃, which was assigned from the association minerals opal-cristobalite (100-150 ℃), quartz-kaolinite (260-280℃), quartz (>300) and alunite group (>250-250 ℃). The assigned temperature is also consistent with the sulfide-sulfate geothermometer that yielded a temperature of 232 ℃ and 240 ℃. Hydrothermal minerals in selectively to pervasively altered ash particles exhibit a typical acid-sulfate and advanced argillic alteration. The advanced argillic alteration is mostly present at near-surface of the geothermal field in calc-alkaline stratovolcanoes. Their presence also gives information a possibly high-temperature vapor zone underneath the volcano.

Mineralogical variation in the volcanic products may reflect the depth explosion or spatial development of advanced argillic alteration below the Ratu Crater. Moreover, it is also presumably affected the oxidized condition at the surface of the volcanic edifice, which

recorded by the presence of jarosite in highly porous ash particles in upper volcanic products. Moreover, recent volcanic eruption possibly related to periodic vapor expansion from magma or intrusion sources, which also may responsible for the complex alteration overprint at the crater-conduit.

References

Alvarado, G., M., Daniela, D., Pierfrancesco, J. M. D., Moor, and A., Geoffroy, 2016. Are the ashes from the latest eruptions (2010–2016) at Turrialba volcano (Costa Rica) related to phreatic or phreatomagmatic events? *Journal of Volcanology and Geothermal Research*. DOI: 10.1016/j.jvolgeores.2016.09.003.

Arribas Jr, A., 1995. Characteristics of high-sulfidation epithermal deposits, and their relation to magmatic fluid. *Mineralogical Association of Canada Short Course*, 23, 419-454.

Ault, W. V. & Jensen, M. L. 1963. Summary of sulfur isotope standards. In M. L. Jensen (ed.). Bio-geochemistry of Sulfur Isotopes, pp. 509– 67. National Science Foundation Symposium Proceedings. Yale University, New Haven

Bajnóczi, B., Hartai, E., and Nagy, G., 2004. Phosphate-bearing minerals in the advanced argillic alteration zones of high-sulphidation type ore deposits in the Carpatho-Pannonian region; Acta Mineralogica-Petrographica Szeged.

Barberi, F., Bertagnini, A., Landi, P., Principe, C., 1992. A review on phreatic eruptions and their precursors *Journal of Volcanology and Geothermal Research*. DOI:

Belousov, M., Belousova, D. Krimer, F. Costa, O. Prambada, and A. Zaennudin, 2015, Volcaniclastic stratigraphy of Gede Volcano, West Java, Indonesia: How it erupted and when; *Journal of Volcanology and Geothermal Research*. DOI: 10.1016/j.jvolgeores.2015.05.018.

Bemmelen, R.W. Van., *1949*. *The Geology of Indonesia*, Vol. 1 A, Government. Printing Office, The Hauge.

Breard, E. C. P., Lube, G., Cronin, S. J., Fitzgerald, R., Kennedy, B., Scheu, B., Montanaro, C. White, J. D. L., Tost, M., Procter, J. N., and Moebis, A. (2014). "Using the spatial distribution and lithology of ballistic blocks to interpret eruption sequence and dynamics: August 6 2012 Upper Te Maari eruption, New Zealand." Journal of Volcanology and Geothermal Research 286: 373-386.

Browne P.R.L. and J.V. Lawless, 2001, Characteristics of hydrothermal eruptions, with examples from New Zealand and elsewhere; *Earth Science Review*, DOI: 10.1016/S0012-8252(00)00030-1

Cashman, K. V., and R. P., Hoblitt, 2004. Magmatic precursors to the 18 May 1980 eruption of Mount St. Helens, USA. *Geology*. DOI: 10.1130/g20078.1

Chatterjee, N.D., Johannes, W., Leistner, H., 1984. The system CaO-Al_2O_3-SiO_2-H_2O: new phase equilibria data, some calculated phase relations, and their petrological applications. Contrib. Mineral. Petrol. 88:1-13.

Curray, J. R., G. G. Shor Jr, R. W. Raitt, and M. Henry, 1977, Seismic refraction and reflection studies of crustal structure of the Eastern Sunda and Western Banda arcs; *Journal of Geophysical Research*. DOI: 10.1029/JB082i017p02479

Center Volcanology and Hazard Mitigation, 2016, Database of volcanoes in Indonesia; CVGHM Report.

Dong, G., Morrison, G., Jaireth, S., 1995. Quartz texture in epithermal veins, Queensland – classification, origin, and implication. Economic Geology 90:1841-1856. doi: 10.2113/gsecongeo.90.6.1841

Dvorak, J., Matahelumual, J., Okamura, A. T., Said, H., Casadevall, T. J., and Mulyadi, D., 1990. Recent uplift and hydrothermal activity at Tangkuban Parahu volcano, West Java, Indonesia; Bulletin of Volcanology, 53(1): 20-28.

Edwards, C. M., 1990, Petrogenesis of tholeiitic, calc-alkaline and alkaline volcanic rocks, Sunda Arc, Indonesia; Ph.D. Thesis, Royal Holloway, University of London.

Fournier, R.O., 1985, The behavior of silica in hydrothermal solution; Review in economic geology, 2, 45-62.

Gasparon, M., D. R., Hilton, and R. Varne, 1994, Crustal contamination processes traced by helium isotopes: Examples from the Sunda arc, Indonesia; *Earth and Planetary Science Letters*. DOI: 10.1016/0012-821X(94)90239-9

Gertisser, R. and J., Keller, 2003, Temporal variations in magma composition at Merapi volcano (Central Java, Indonesia): magmatic cycles during the past 2000 years of explosive activity; *Journal of Volcanology and Geothermal Research*. DOI: 10.1016/S0377-0273(03)00025-8

Gertisser, R., and J. Keller, 2003, Trace element and Sr, Nd, Pb and O isotopic variations in the medium-K and high-K volcanic rocks from Merapi Volcano, Central Java, Indonesia: evidence for the involvement of subducted sediments in the Sunda Arc magma genesis; *Journal of Petrology*. DOI: 10.1093/petrology/44.3.457

Hadikusumo, D., 1961, Report of the volcanological research and volcanic activity for the period 1950-1957; Bulletin Volcanology Survey Indonesia, 111, 112.

Hadisantono, R.S., Juwarna, H., and Seotoyo, 1986, Geologic map of Tangkuban Parahu Volcano, Bandung, West Java; Volcanological survey Indonesia, Bandung, Open-File Map 1:50000

Handley, H. K., 2006, Geochemical and Sr-Nd-Hf-O isotopic constraints on volcanic petrogenesis at the Sunda Arc, Indonesia; Ph.D. thesis, Durham University.

Handley, H. K., S., Turner, C. G., Macpherson, R., Gertisser, and & J. P., Davidson, 2011, Hf-Nd isotope and trace element constraints on subduction inputs at island arcs: Limitations of Hf anomalies as sediment input indicators; *Earth and Planetary Science Letters*. DOI: 10.1016/j.epsl.2011.01.034

Hall, R., 2002, Cenozoic geological and plate tectonic evolution of SE Asia and the SW Pacific: Computer-based reconstructions, model and animations; *Journal of Asian Earth Sciences*. DOI: 10.1016/S1367-9120(01)00069-4

Hall, R., and H. Smyth, 2008, Cenozoic arc processes in Indonesia: identification of the key influences on the stratigraphic record in active volcanic arcs; *Geological Society of London*. DOI: 10.1130/2008.2436(03)

Henley, R. W., and B. R., Berger, 2011. Magmatic-vapor expansion and the formation of high-sulfidation gold deposits: Chemical controls on alteration and mineralization; *Ore Geology Reviews*. DOI: 10.1016/j.oregeorev.2010.11.003

Hemley, J.J., Montoya, J.W., Marinenko, J.W., Luce, R.W., 1980. Equilibria in the system Al_2O_3-SiO_2-H_2O and some general implications for alteration/mineralisation processes. Econ. Geol. 75:210-228.

Heiken, G., and Wohletz, K., 1985. *Volcanic ash*. University Presses of California, Chicago, Harvard, and MIT.

Hedenquist JW, Arribas A, and Reynolds, TJ, 1998. Evolution of an intrusion-centered hydrothermal system: Far Southeast-Lepanto porphyry and epithermal Cu–Au deposits, Philippines. Econ Geol 93:373–404

Hedenquist, J., and Y., Taran, 2013. Modeling the formation of advanced argillic lithocaps: volcanic vapor condensation above porphyry intrusions. *Economic Geology*. DOI:10.2113/econgeo.108.7.1523.

Jamtveit, B., H., Svensen, Y. Y., Podladchikov, and S., Planke, 2004. Hydrothermal vent complexes associated with sill intrusions in sedimentary basins. In: Breitkreuz, C. & Petford, N. (eds) Physical Geology of High-Level Magmatic Systems. *Geological Society of London, Special Publications*. DOI: 10.1144/GSL.SP.2004.234.01.15

John, D.a., Sisson, T.W., Breit, G.N., Rye R.O., and Valance, J.W., 2008, Characteristics, extent and origin of hydrothermal alteration at Mount Rainier volcano, Cascades Arc, USA: Implications for debris-flow hazards and mineral deposits. Journal volcanology and geothermal research, 175, 289-314.

Kartadinata, M. N., M., Okuno, T., Nakamura, and T. Kobayashi, 2002, Eruptive history of Tangkuban Parahu Volcano, West Java, Indonesia: A preliminary report; *Journal of Geography*, 111, 404-409.

Kartadinata, M.N., 2005, Tephrochronological study on eruptive history of Sunda-Tangkuban Perahu volcanic complex, West Java, Indonesia. Doctoral Dissertation, Kagoshima University.

Kusumadinata, K. (1979). Database of volcanoes in Indonesia. Volcanological Survey Indonesia, Bandung, pp 820.

Laetsch T., and Downs R., 2006, Software for identification and refinement of cell parameter from powder diffraction data of minerals using the RRUFF Project and American Mineralogist Crystal Structure Databases. Abstracts from the 19th general meeting of the International Mineralogical Association, Kobe, Japan, 23-28 July 2006.

Li, G., D. R., Peacor, E. J., Essene, D. R., Brosnahan, and R. E., Beane, 1992. Walthierite $Ba_{0.5}\square_{0.5}Al_3(SO_4)_2(OH)_6$ and huangite $Ca_{0.5}\square_{0.5}Al_3(SO_4)_2(OH)_6$, two new minerals of the alunite group from the Coquimbo region, Chile; *American Mineralogist*. 77, 1275-1284.

Lowenstern, J. B., V., van Hinsberg, K., Berlo, M., Liesegang, K. Iacovino, I. N., Bindeman, and H. M., Wright, 2018. Opal-A in Glassy Pumice, Acid Alteration, and the 1817 Phreatomagmatic Eruption at Kawah Ijen (Java), Indonesia. *Frontiers in Earth Science*. DOI: 10.3389/feart.2018.00011.

Mazot, A., Bernard, A., Fischer, T., Inguaggiato, S., and Sutawidjaja, I. S., 2008. Chemical evolution of thermal waters and changes in the hydrothermal system of Papandayan volcano (West Java, Indonesia) after the November 2002 eruption; Journal of Volcanology and Geothermal Research 178(2): 276-286.

Minami, Y., Imura, T., Hayashi, S., and Ohba, T., 2016, Mineralogical study on volcanic ash of the eruption on September 27, 2014 at Ontake volcano, central Japan: correlation with porphyry copper systems; Earth, Planets and Space,v. 68, p. 67, DOI: 10.1186/s40623-016-0440-2.

Maeno, F., S. Nakada, T. Oikawa, M. Yoshimoto, J. Komori, Y. Ishizuka, Y. Takeshita, T. Shimano, T. Kaneko, and M. Nagai, 2016. Reconstruction of a phreatic eruption on 27 September 2014 at Ontake volcano, central Japan, based on proximal pyroclastic density current and fallout deposits; *Earth, Planets, and Space*. DOI: 10.1186/s40623-016-0449-6

Martini, M., 1996. Chemical characters of the gaseous phase in different stages of volcanism: precursors and volcanic activity; *Scarpa, R., Tilling, R. (Eds.), Monitoring and mitigation of volcano hazards*, pp. 199–219.

McPhie, J., M., Doyle, and R., Allen, 1993. *Volcanic textures: a guide to the interpretation of textures in volcanic rocks*. Hobart, Tas: Centre for Ore Deposit and Exploration Studies, University of Tasmania.

Miyabuchi, Y., 2015. Identification of paleosols around volcanoes dominating long-term small ash emissions: a case study from Aso Volcano, Japan; Special section determination of the construction of an outcrop database to reveal Eruptive History, Bulletin of the Volcanological Society of Japan, v. 60, p. 173-180. DOI: 10.18940/kazan.60.2_173 (written in Japanese with English abstract)

Minami, Y., T. Imura, S. Hayashi, and T. Ohba, 2016. Mineralogical study on volcanic ash of the eruption on September 27, 2014 at Ontake volcano, central Japan: correlation with porphyry copper systems; *Earth, Planets, and Space*. DOI: 10.1186/s40623-016-0440-2.

Nasution, A., Kartadinata, M. N., Kobayashi, T., Siregar, D., Sutaningsih E., Hadisantono, R., Kadarstia, 2004. Geology, age dating, and geochemistry of the Tangkuban Parahu Geothermal Area, West Java, Indonesia; Journal Geothermal Resource Society of Japan.

Nicholls, I. A. and D. J., Whitford, 1976, Primary magmas associated with Quaternary volcanism in the western Sunda Arc, Indonesia; *Volcanism in Australasia*, 77-89.

Nicholls, I. A., D. J., Whitford, K. L. Harris, and S. R.. Taylor, 1980, Variation in the geochemistry of mantle sources for tholeiitic and calc-alkaline mafic magmas, western Sunda volcanic arc, Indonesia; *Chemical Geology*. DOI: 10.1016/0009-2541(80)90105-9

Oikawa, T., T., Ohba, A., Fujinawa, and H., Sasaki, 2018. Geological study of phreatic eruptions, The Journal of the Geological Society of Japan, DOI: 10.5575/geosoc.2017.0071

Oikawa, T., Y., Mitsuhiro, N., Setsuya, M., Fukashi, K., Jiro, S., Taketo, T., Yoshihiro, I., Yoshihiro, and I., Yasuhiro, 2016. Reconstruction of the 2014 eruption sequence

of Ontake Volcano from recorded images and interviews. *Earth, Planets, and Space*. DOI: 10.1186/s40623-016-0458-5

Ohba, T., H., Taniguchi, T., Miyamoto, S., Hayashi, and T., Hasenaka, 2007. Mud plumbing system of an isolated phreatic eruption at Akita Yakeyama volcano, northern Honshu, Japan; *Journal of Volcanology and Geothermal Research*. DOI: 10.1016/j.jvolgeores.2006.11.001

Ohba, T., and Y. Kitade, 2005. Subvolcanic hydrothermal systems: Implications from hydrothermal minerals in hydrovolcanic ash, *Journal of Volcanology and Geothermal Research*. DOI: 10.1016/j.jvolgeores.2005.02.002

Pardo, N., S. J., Cronin, K., Németh, M., Brenna, C. I., Schipper, E., Breard, J. D. L., Whitte, J., Procter, B., Stewart, J., Augustin-Flores, A., Moebis, A., Zernack, G., Kereszturi, G., Lube, A., Auer, V., Neall, and C., Wallace, 2014. Perils in distinguishing phreatic from phreatomagmatic ash: insights into the eruption mechanisms of the 6 August 2012 Mt. Tongariro eruption, New Zealand; Journal of Volcanology and Geothermal Research. 286, 397–414. DOI: 10.1016/j.jvolgeores.2014.05.001

Reed, H. M., 1997. Hydrothermal alteration and its relationship to ore fluid composition; in *Geochemistry of Hydrothermal Ore Deposit*, John Willey & Son Inc.

Rye, R.O., Bethke, P.M., Wasserman, M.D., 1992. The stable isotope geochemistry of acid sulfate alteration; Economic Geology 87:225-262. doi: 10.2113/gsecongeo.87.2.225

Rye, R.O., 1993. The evolution of magmatic fluids in the epithermal environment: the stable isotope perspective; Economic Geology 88:733–752

Sakuyama, M. (1979). Evidence of magma mixing: petrological study of Shiruma-Oike calc-alkaline andesite volcano, Japan; *Journal of Volcanology and Geothermal Research*, vol. 5, 179-208.

Sakuyama, M. (1981). Petrological study of the Myoko and Kurohime volcanoes, Japan: crystallization sequence and evidence for magma mixing; *Journal of Petrology*, vol. 22, 553-583.

Sanno, Y., T., N.., Kagoshima, Y., Takahata, E., Hishio, D. L., Roulleau, T., Pinti, and P., Fischer, 2015. Ten-year helium anomaly prior to the 2014 Mt Ontake eruption; *Science Report*. DOI: 10.1038/srep13069.

Scher, S., Williams-Jones, A., and Williams-Jones, G., (2013). Fumarolic Activity, Acid-Sulfate Alteration, and High Sulfidation Epithermal Precious Metal Mineralization in the Crater of Kawah Ijen Volcano, Java, Indonesia; Economic geology, doi: 10.2113/econgeo.108.5.1099.

Sendjaja, Y. A., Kimura, J.-I., & Sunardi, E. (2009). Across-arc geochemical variation of Quaternary lavas in West Java, Indonesia: Mass-balance elucidation using arc basalt simulator model; *Island Arc*. DOI: 10.1111/j.1440-1738.2008.0.0641.x

Sillitoe, R. H., 2010. Porphyry copper system; Economic Geology, 105, 3-41.

Silitonga, P.H., 1973, Peta Geologi Lembar Bandung, Djawa; Geologic map of the Bandung quadrangle, Java. Geology Survey Indonesia, Ministry of Mines, scale 1:100000.

Stehn, C. E., 1929, Tangkoeban Prahoe: excursion guide B.3 VI; *Pacific Asian Congress*, Bandung, 22 pp.

Soetoyo, and Hadisantono, 1992. Geological map of Tangkuban Parahu Volcano/Sunda Complex Volcano, West Java. Centre of Volcanological and Geology Hazard (CVGHM), Indonesia.

Sunardi, E., and J. Kimura, 1998. Temporal chemical variation in late cenozoic volcanic rocks around Bandung Basin, West Java, Indonesia; *Journal Mineralogy, Petrology, Economic Geology*, 93, 103-128.

Stoffregen, R., 1987. Genesis of acid-sulfate alteration and Au-Cu-Ag mineralization at Summitville, Colorado. Economic Geology 82:1575-1591. doi: 10.2113/gsecongeo.82.6.1575

Stoffregen, R.E., and Alpers, C.N., 1987, Woodhouseite and svanbergite in hydrothermal ore deposits: Products of apatite destruction during advanced argillic alteration: Canadian Mineralogist, v. 25, p. 201–211.

Stoffregen, R. E., C. N. Alpers, J. L. Jambor; Alunite-Jarosite Crystallography, Thermodynamics, and Geochronology. *Reviews in Mineralogy and Geochemistry*; 40 (1): 453–479. doi: 10.2138/rmg.2000.40.9

Sutopo, B., 2013. The Martabe Au-Ag high-sulfidation epithermal deposits, Sumatra, Indonesia: implication from ore genesis and exploration, PhD thesis, University of Tasmania.

Suzuki, Y., M., Nagai, F., Maeno, A., Yasuda, N., Hokanishi, T., Shimano, M., Ichihara, T., Kaneko, and S., Nakada, 2013. Precursory activity and evolution of the 2011 eruption of Shinmoe-dake in Kirishima volcano-insights from ash samples; Earth, Planets, and Space. 65, 591–607. DOI: 10.5047/eps.2013.02.004

Suryo, I., 1981. *Report of the volcanic activity in Indonesia for the period 1961-1963*. Bull Volcanological Survey Indonesia, Bandung No 104:116 pp

Suryo, I., 1985. *Report of the volcanic activity in Indonesia for the period 1964-1970*. Bull Volcanological Survey Indonesia, Bandung No 106:150 pp

Syahidan, A. A., Suryantini, A., Susanto, and A., Nurdiana, 2015. Hydrothermal alteration study of Tangkuban Parahu Craters, and its implication to geothermal conceptual model. Proceeding Indonesia International Geothermal Convention and Exbition, Jakarta.

Tregoning, P., F. K., Brunner, Y., Bock, S. S., Puntodewo, R., McCaffrey, and J. F., Genrich, 1994. First geodetic measurement of convergence across the Java Trench; Geophysical Research Letters. DOI: 10.1029/94GL01856

Van Hinsberg V, Berlo K, van Bergen M, Williams-Jones A, 2010a. Extreme alteration by hyperacidic brines at Kawah Ijen volcano, East Java, Indonesia: I. Textural and mineralogical imprint, vol 198, pp 253–263. doi:10.1029/2012GC004192

Watanabe, Y., and E., Ohta, 2005. Polymetallic Pb-Zn-Ag-In Toyoha Deposit; geology, style, genesis, and exploration, Institue for Geo-Resources and Environment, AIST, Tsukuba, Japan.

Watanabe, Y. and J., Hedenquist, 2001. Mineralogical and stable isotope zonation at the surface over the El Salvador porphyry Cu deposit, Chile. Economic Geology. 96. 1775-1797. 10.2113/96.8.1775.

Widiyantoro, S., Pesicek, J. D., & Thurber, C. H. (2011). Subducting slab structure below the eastern Sunda arc inferred from non-linear seismic tomographic imaging. *Geological Society, London, Special Publications*. DOI: 10.1144/SP355.7

Whitford, D. J. (1975). Strontium isotopic studies of the volcanic rocks of the Sunda arc, Indonesia, and their petrogenetic implications; *Geochimica et Cosmochimica Acta*. DOI: 10.1016/0016-7037(75)90136-2

Wheller, G. E., Varne, R., Foden, J. D., & Abbot, M. J. (1987). Geochemistry of Quaternary volcanism in the Sunda-Banda arc, Indonesia, and three-component genesis of island arc basaltic magmas; *Journal of Volcanology and Geothermal Research*. DOI: 10.1016/0377-0273(87)90041-2

Wohletz, K. and G. *Heiken*, 1992. *Volcanology and Geothermal Energy*. Berkeley: University of California Press.

Yanagisawa F, Sakai H (1983) Thermal decomposition of barium sulfate-vanadium pentaoxide-silica glass mixtures for preparation of sulfur dioxide in sulfur isotope ratio measurements. Analytical Chemistry 55:985–987

Appendices Chapter 3

Total observation in SEM observation;

Sample ID	Silica (opal, cristobalite, quartz)	Silica alunite	Silica+alunite ±Kaolinite	Alunite Jarosite	Altered glass	Unaltered	Total
TP01	5	6	3	0	0	0	14
TP05	5	10	12	0	0	0	27
TP07	10	3	7	0	0	0	20
TP08	8	6	4	10	0	5	33
TP09	7	4	4	0	0	0	15
TP10	3	4	2	0	0	8	17
TP11	6	2	6	0	0	2	16
TP13	4	12	8	0	7	0	31
TP15	10	11	10	0	0	0	31
TP17	6	3	2	0	8	0	19
TP19	5	8	7	0	3	7	30
TP21	12	7	3	0	0	0	22
TP22	4	12	4	0	0	3	23
TP24	10	7	9	0	0	0	26
TP25	7	6	7	0	0	7	27
Total	102	101	88	10	18	32	351
Ratio of alunite alteration and total observation			56.56%				
Ratio of silica alteration and total observation			29.95%				

The representative of microprobe analyses of alunite from SEM-EDS;

ID:	1	2	3	4	5	6	7	8	9	10	11	12	13	14	15	16	17	18
Mineral:	Alu	Alu	Alu	Alu	Alu	Alu	Alu	Alu	Alu	Alu	Alu	Alu	Alu	Alu	Alu	Alu	Alu	Alu
Al_2O_3	31.70	35.35	37.86	37.71	38.77	38.02	40.36	41.10	39.69	39.24	39.37	37.84	39.07	38.48	39.08	37.95	32.58	30.90
CaO	0.48	0.41	0.29	0.27	0.29	0.30	0.28	0.42	0.32	0.15	0.31	0.44	0.39	0.16	0.18	0.26	0.22	0.24
Na_2O	0.95	1.18	0.90	0.80	0.49	0.44	0.38	0.27	0.21	0.24	0.24	0.26	0.27	0.50	0.45	0.38	0.33	0.47
K_2O	5.47	5.74	3.43	3.39	4.35	4.63	4.38	4.11	4.43	4.60	3.94	3.83	3.54	3.99	3.57	3.66	4.13	5.11
P_2O_5	1.75	1.36	0.39	0.19	0.49	1.00	1.23	1.30	1.41	1.04	1.17	1.36	1.32	1.05	1.15	0.80	1.23	1.46
SO_3	42.56	49.03	54.00	55.18	55.68	53.85	55.07	56.10	56.27	54.57	53.20	52.28	53.66	52.90	54.19	52.02	44.98	44.52
As_2O_3	0.11	0.27	0.15	0.12	0.16	0.13	0.01	0.14	0.39	0.23	0.09	0.17	0.18	0.13	0.18	0.07	0.22	0.17
Total	83.02	93.34	97.02	97.66	100.23	98.37	101.71	103.44	102.72	100.07	98.32	96.18	98.43	97.21	98.80	95.14	83.69	82.87
Formula based on 11 oxygen atoms																		
Al	2.35	2.54	2.55	2.51	2.53	2.54	2.61	2.61	2.55	2.58	2.63	2.59	2.60	2.60	2.59	2.61	2.58	2.49
Ca	0.03	0.03	0.02	0.02	0.02	0.02	0.02	0.02	0.02	0.01	0.02	0.03	0.02	0.01	0.01	0.02	0.02	0.02
Na	0.12	0.14	0.10	0.09	0.05	0.05	0.04	0.03	0.02	0.03	0.03	0.03	0.03	0.06	0.05	0.04	0.04	0.06
K	0.44	0.45	0.25	0.24	0.31	0.34	0.31	0.28	0.31	0.33	0.28	0.28	0.26	0.29	0.26	0.27	0.35	0.45
P	0.21	0.16	0.04	0.02	0.05	0.11	0.13	0.13	0.15	0.11	0.13	0.15	0.14	0.11	0.12	0.09	0.16	0.19
S	2.01	2.25	2.31	2.34	2.32	2.30	2.27	2.27	2.30	2.29	2.26	2.28	2.28	2.28	2.29	2.28	2.27	2.29
Total	5.16	5.57	5.28	5.23	5.29	5.36	5.38	5.35	5.34	5.35	5.35	5.36	5.33	5.35	5.32	5.32	5.42	5.50

Gray marked indicates a total of mineral chemistry (too low or high).

A) Backscattered electron image showing zoned alunite on the vesicle wall. B) K_2O, Na_2O, and CaO compositions from zoned alunite, which was obtained from EDS. Compositions are identical with all alunite minerals that occur as a fracture filling.

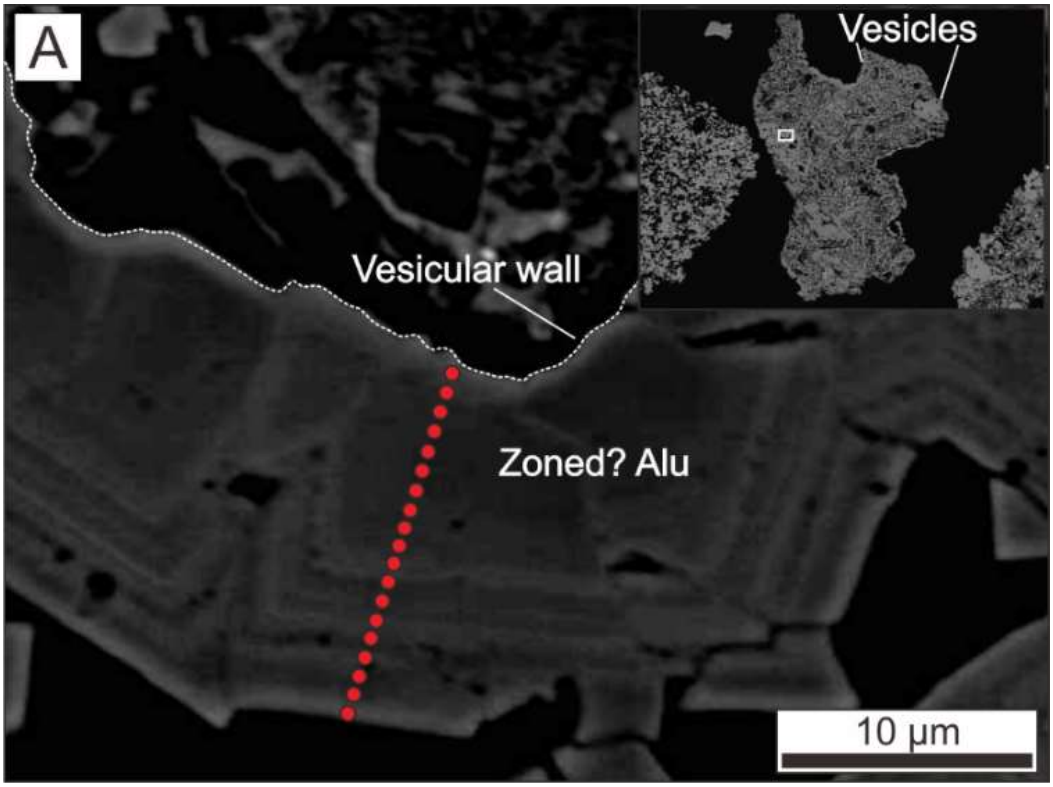

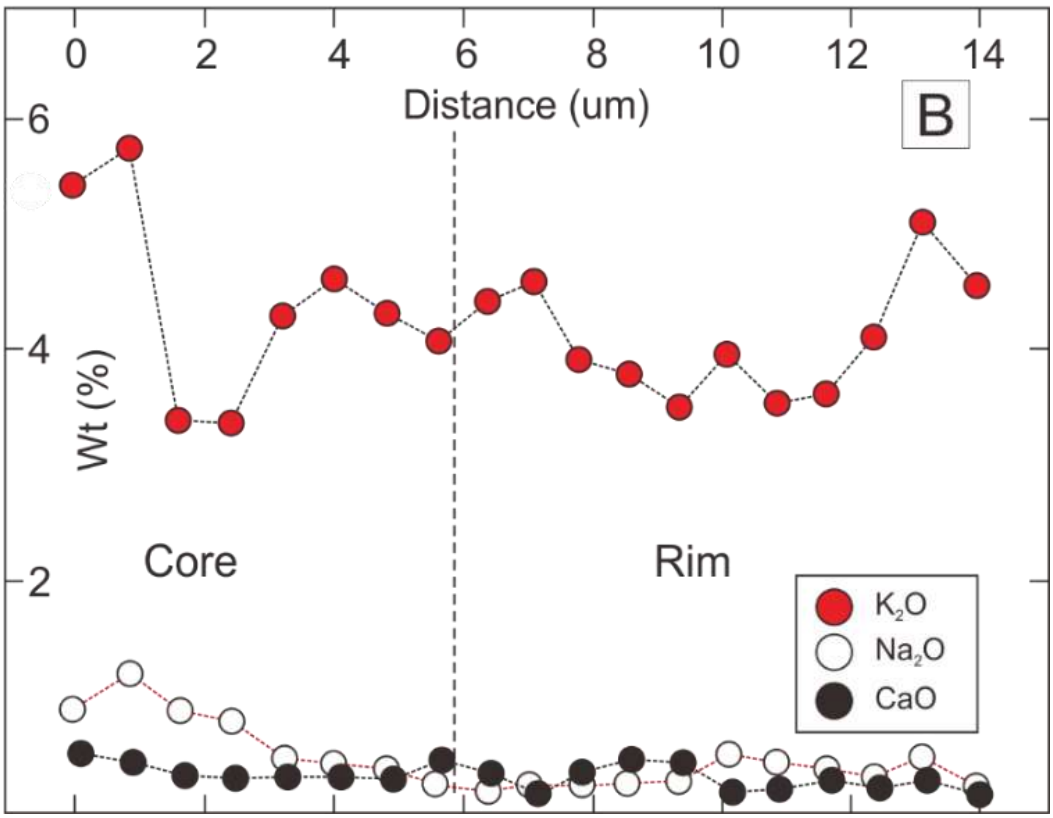

The representative of microprobe analyses of sanidine from SEM-EDS

ID:	1	2	3	4	5	6	7	8	9	10	11	12	13
Mineral:	Sa	Sa	Sa	Sa	Sa	Sa	Sa	Sa	Sa	Sa	Sa	Sa	Sa
SiO_2	65.60	64.67	65.91	65.91	66.21	65.41	65.27	65.35	65.53	65.37	65.47	65.56	64.94
Al_2O_3	18.57	19.80	19.07	19.07	18.53	18.71	19.11	18.61	18.30	18.69	18.87	18.48	19.11
CaO	0.78	0.73	0.66	0.66	0.42	0.63	1.02	0.55	0.50	0.77	0.64	0.34	0.86
Na_2O	4.08	3.55	3.41	3.90	4.15	4.47	5.20	4.45	4.17	4.68	4.34	4.28	2.67
K_2O	11.16	9.47	11.41	11.41	11.28	10.55	8.93	10.56	11.02	9.93	10.49	11.04	13.49
Total	100.19	98.22	100.46	100.95	100.59	99.77	99.53	99.52	99.52	99.44	99.81	99.70	101.07
Formula based on 8 oxygen atoms													
Si	2.98	2.96	2.98	2.97	3.00	2.98	2.96	2.98	3.00	2.98	2.98	2.99	2.96
Al	1.00	1.07	1.02	1.01	0.99	1.00	1.02	1.00	0.99	1.00	1.01	0.99	1.03
Ca	0.04	0.04	0.03	0.03	0.02	0.03	0.05	0.03	0.02	0.04	0.03	0.02	0.04
Na	0.36	0.32	0.30	0.34	0.36	0.39	0.46	0.39	0.37	0.41	0.38	0.38	0.24
K	0.65	0.55	0.66	0.66	0.65	0.61	0.52	0.62	0.64	0.58	0.61	0.64	0.78
Total	5.02	4.94	4.99	5.02	5.02	5.02	5.01	5.02	5.02	5.01	5.01	5.02	5.04
#an	0.04	0.04	0.03	0.03	0.02	0.03	0.05	0.03	0.02	0.04	0.03	0.02	0.04
#or	0.62	0.61	0.67	0.64	0.63	0.59	0.50	0.59	0.62	0.56	0.60	0.62	0.74
#ab	0.34	0.35	0.30	0.33	0.35	0.38	0.50	0.38	0.36	0.40	0.37	0.36	0.22

The representative of microprobe analyses of altered plagioclase from SEM-EDS;

ID:	1	2	3	4	5	6	7	8	9	10	11	12
Mineral:	Altered plagioclase											
SiO_2	87.39	85.39	81.48	87.98	84.50	88.85	90.36	88.44	86.53	84.23	88.44	90.36
TiO_2	0.82	1.35	0.00	0.00	0.00	0.00	0.00	0.00	0.00	0.00	0.00	0.00
Al_2O_3	3.17	3.89	3.52	1.95	2.50	1.81	2.71	0.00	2.72	2.55	1.98	2.71
FeO	0.00	0.00	0.00	0.00	0.00	0.07	0.00	0.00	0.00	0.00	0.00	0.00
CaO	0.20	0.47	0.00	0.61	0.47	0.13	0.07	0.07	0.06	0.18	0.07	0.07
Na_2O	0.50	0.30	0.00	0.20	0.35	0.10	0.04	0.08	0.06	0.02	0.08	0.04
K_2O	0.60	0.35	0.00	0.39	0.43	0.16	0.35	0.49	0.37	0.31	0.49	0.35
Total	92.68	91.75	85.00	91.13	88.25	91.12	93.53	89.08	89.74	87.29	91.06	93.53
Formula based on 8 oxygen atoms												
Si	3.83	3.78	3.85	3.90	3.87	3.92	3.89	3.99	3.88	3.89	3.91	3.89
Ti	0.03	0.04	0.00	0.00	0.00	0.00	0.00	0.00	0.00	0.00	0.00	0.00
Al	0.16	0.20	0.20	0.10	0.14	0.09	0.14	0.00	0.14	0.14	0.10	0.14
Ca	0.01	0.02	0.00	0.03	0.02	0.01	0.00	0.00	0.00	0.01	0.00	0.00
Na	0.04	0.03	0.00	0.02	0.03	0.01	0.00	0.01	0.01	0.00	0.01	0.00
K	0.03	0.02	0.00	0.02	0.03	0.01	0.02	0.03	0.02	0.02	0.03	0.02
Total	4.10	4.10	4.05	4.07	4.09	4.04	4.05	4.03	4.06	4.05	4.05	4.05

The representative of microprobe analyses of fresh plagioclase from SEM-EDS

ID:	1	2	3	4	5	6	7	8	9	10	11	12	13
Mineral:	Fresh plagioclase												
SiO_2	56.74	56.67	57.19	54.99	55.22	53.44	54.71	55.59	54.15	54.45	53.10	58.31	61.25
Al_2O_3	27.25	26.08	26.99	27.20	27.44	28.45	27.87	26.60	28.11	28.10	28.86	23.31	24.00
FeO	0.65	0.82	0.61	0.60	0.70	0.96	0.63	0.79	0.96	0.98	0.00	1.42	0.00
CaO	10.79	9.87	9.82	10.61	11.09	12.29	11.55	10.30	11.70	11.72	12.03	7.50	6.82
Na_2O	5.53	5.55	5.63	5.02	4.80	4.31	4.54	5.04	4.48	4.60	4.26	5.88	5.96
K_2O	0.64	0.72	0.73	0.57	0.72	0.56	0.62	0.82	0.60	0.63	0.43	1.62	2.17
Total	101.60	99.71	100.97	98.99	99.97	100.01	99.92	99.27	100.00	100.48	98.68	98.04	100.20
Formula based on 8 oxygen atoms													
Si	2.50	2.53	2.55	2.56	2.53	2.50	2.43	2.48	2.53	2.46	2.46	2.43	2.68
Al	1.47	1.43	1.43	1.41	1.44	1.47	1.53	1.49	1.43	1.51	1.50	1.56	1.26
Fe^{+2}	0.00	0.02	0.02	0.02	0.02	0.03	0.04	0.02	0.03	0.04	0.04	0.00	0.05
Ca	0.56	0.52	0.48	0.47	0.49	0.54	0.60	0.56	0.50	0.57	0.57	0.59	0.37
Na	0.44	0.48	0.49	0.49	0.47	0.42	0.38	0.40	0.45	0.39	0.40	0.38	0.52
K	0.03	0.04	0.04	0.04	0.04	0.04	0.03	0.04	0.05	0.03	0.04	0.03	0.10
Total	5.00	5.01	5.00	5.00	5.00	5.00	5.01	4.99	4.99	5.00	5.01	4.99	4.99
#an	0.54	0.50	0.48	0.47	0.49	0.54	0.59	0.56	0.50	0.57	0.56	0.59	0.37
#or	0.03	0.04	0.04	0.04	0.04	0.04	0.03	0.04	0.05	0.03	0.04	0.03	0.10
#ab	0.43	0.46	0.49	0.49	0.47	0.42	0.38	0.40	0.45	0.40	0.40	0.38	0.53

Graph showing the atomic per unit formula of plagioclase cation against silica atom per formula unit based on oxygen atom of 8 .

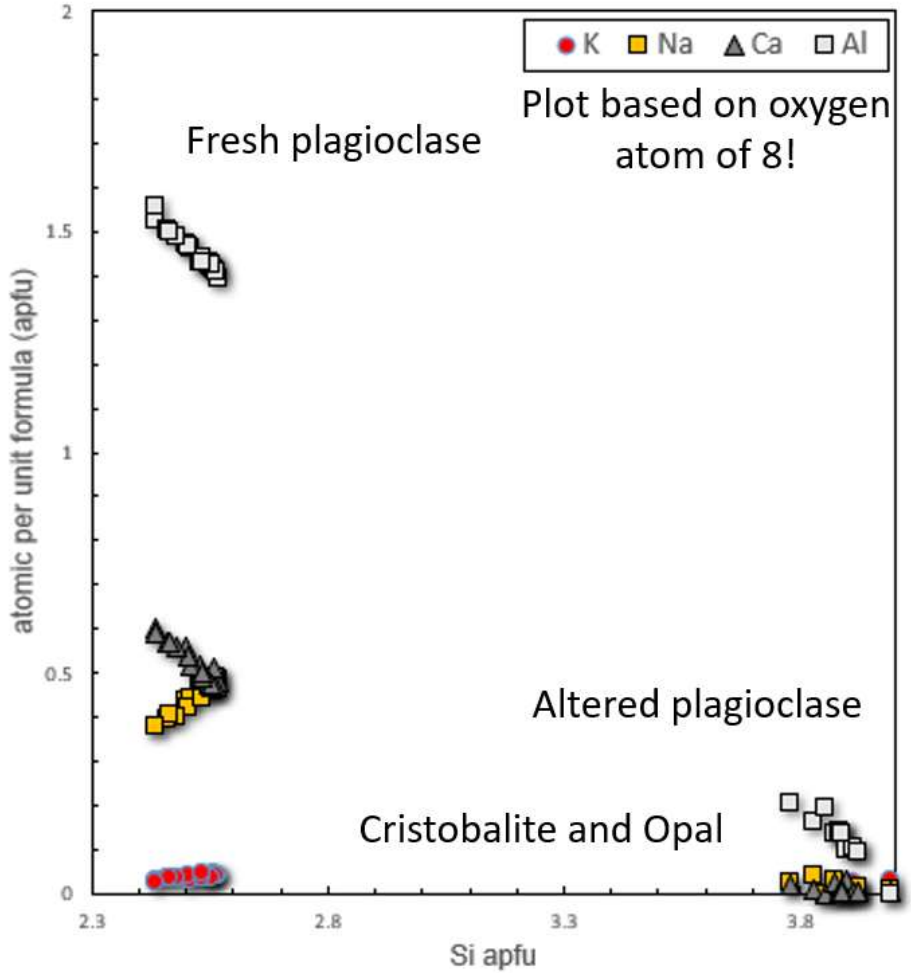

Equation of sulfide-sulfate geothermometer;

$$1000 \ln \alpha_{SO_4-H_2S} = 6.463 \times {}^{10^6}/_{T^2} + 0.56 \qquad \text{(Ohmoto and Lasaga, 1982)}$$

$$1000 \ln \alpha_{FeS_2-H_2S} = 0.4 \times {}^{10^6}/_{T^2} \qquad \text{(Ohmoto and Rye, 1979)}$$

Equation (3) and (4) were subtracted to produce a representative sulfate-sulfide geothermometer formula, by the following;

$$1000 \ln \alpha_{SO_4-FeS_2} = 6.063 \times {}^{10^6}/_{T^2} + 0.56$$